Biomaterials 294 (2023) 121999

Contents lists available at ScienceDirect

Biomaterials

journal homepage: www.elsevier.com/locate/biomaterials

Electrically stimulated 3D bioprinting of gelatin-polypyrrole hydrogel with dynamic semi-IPN network induces osteogenesis via collective signaling and immunopolarization

Sayan Deb Dutta [a], Keya Ganguly [a], Aayushi Randhawa [a,b], Tejal V. Patil [a,b], Dinesh K. Patel [c], Ki-Taek Lim [a,b,c,d,*]

[a] Department of Biosystems Engineering, Kangwon National University, Chuncheon, 24341, Republic of Korea
[b] Interdisciplinary Program in Smart Agriculture, Kangwon National University, Chuncheon, 24341, Republic of Korea
[c] Institute of Forest Sciences, Kangwon National University, Chuncheon, 24341, Republic of Korea
[d] Biomechagen Co., Ltd., Chuncheon, 24341, Republic of Korea

ARTICLE INFO

Keywords:
Conductive hydrogels
3D bioprinting
Direct ink writing
Non-Newtonian flow
Ex-vivo printing
Osteogenesis

ABSTRACT

In recent years, three-dimensional (3D) bioprinting of conductive hydrogels has made significant progress in the fabrication of high-resolution biomimetic structures with gradual complexity. However, the lack of an effective cross-linking strategy, ideal shear-thinning, appropriate yield strength, and higher print fidelity with excellent biofunctionality remains a challenge for developing cell-laden constructs, hindering the progress of extrusion-based 3D printing of conductive polymers. In this study, a highly stable and conductive bioink was developed based on polypyrrole-grafted gelatin methacryloyl (GelMA-PPy) with a triple cross-linking (thermo-photo-ionically) strategy for direct ink writing-based 3D printing applications. The triple-cross-linked hydrogel with dynamic semi-inner penetrating polymer network (semi-IPN) displayed excellent shear-thinning properties, with improved shape fidelity and structural stability during 3D printing. The as-fabricated hydrogel ink also exhibited "plug-like *non-Newtonian*" flow behavior with minimal disturbance. The bioprinted GelMA-PPy-Fe hydrogel showed higher cytocompatibility (93%) of human bone mesenchymal stem cells (hBMSCs) under microcurrent stimulation (250 mV/20 min/day). Moreover, the self-supporting and tunable mechanical properties of the GelMA-PPy bioink allowed 3D printing of high-resolution biological architectures. As a proof of concept, we printed a full-thickness rat bone model to demonstrate the structural stability. Transcriptomic analysis revealed that the 3D bioprinted hBMSCs highly expressed gene hallmarks for *NOTCH*/mitogen-activated protein kinase (*MAPK*)/*SMAD* signaling while down-regulating the *Wnt*/*β*-Catenin and epigenetic signaling pathways during osteogenic differentiation for up to 7 days. These results suggest that the developed GelMA-PPy bioink is highly stable and non-toxic to hBMSCs and can serve as a promising platform for bone tissue engineering applications.

1. Introduction

Three-dimensional (3D) biomimetic scaffolds that support stem cell growth and differentiation have long been studied as promising tools for tissue engineering and regenerative medicine [1]. Unlike traditional tissue engineering scaffolds, 3D printing or "additive manufacturing" has expanded rapidly to re-create native tissue structures and organs [2]. The 3D printing approach deals with rapid prototyping and precision, making multi-material objects implantable for tissue regeneration without toxic effects on the human body [3]. In bone tissue engineering, 3D printing holds great promise for developing precisely printable and implantable bone constructs intended to heal bone-related disorders, such as bone fractures, inflammation, and tumor therapy [4,5]. Additionally, 3D bioprinting helps re-create the native extracellular niche that favors stem cell growth in 3D form and uses it as a template for cell proliferation and differentiation [6,7].

Currently, conductive biopolymers are extensively used to study stem cell growth in the presence of electrical stimulation [8,9]. Although the 3D printing of conductive biopolymers has been well elucidated in the literature, practical applications remain challenging owing to the

* Corresponding author. Department of Biosystems Engineering, Kangwon National University, Chuncheon, 24341, Republic of Korea.
E-mail address: ktlim@kangwon.ac.kr (K.-T. Lim).

https://doi.org/10.1016/j.biomaterials.2023.121999
Received 3 August 2022; Received in revised form 30 December 2022; Accepted 8 January 2023
Available online 14 January 2023

difficulty in electrical stimulation of culture cells for a longer time. The 3D printing of electroactive biopolymers relies on the continuous and steady flow of hydrogel ink, rapid curing, and higher print fidelity when deposited on the printing platform. To date, numerous UV-curable bioinks, in combination with metal nanoparticles, have been used to develop conductive scaffolds. Among the several conductive materials, carbon nanotubes, graphene oxide (GO), polyaniline (PANI), and polypyrrole (PPy) have been used because of their excellent electrical conductivity, making them ideal for the electrical stimulation of cells, drug delivery, and neural tissue regeneration [10]. The biofabrication of conductive polymers mostly relied on conventional manufacturing techniques such as soft lithography [11,12], ink-jet printing [13,14], screen printing [15], aerosol printing [16], and electrochemical patterning [15,17] with limitations and challenges. The existing manufacturing technique allowed low-resolution (~100–400 μm), poor quality (low shape fidelity), and high-cost printing processes (photo--patterning, masking, etching, and post-curing), desirable mechanical strength, slow biodegradation, therefore hindering the current application of conductive biopolymers in 3D printing [15]. In particular, the use of 3D bioprinted conductive hydrogels with higher shape fidelity, conductivity, controlled biodegradability with superior mechanical property is ill-explored for tissue engineering application. For example, GO, silver, polythiophene, polypyrrole, and MXene-based 3D printed conductive hydrogels has been reported with robust mechanical (~0.02–1.27 MPa) and electrical conductivity (~0.05–10^4 S m^{-1}) without any fare evidence of bioprinting [18–22]. Most of 3D printable inks composed of metals, liquid metals, liquid crystals, cell-laden bioinks, bioactive glass, soft elastomers, and magnetic nanocomposites have been expanded as bioink library [15,23–25]. However, a little progress has been devoted to 3D printing of conductive biopolymers. Therefore, most of present studies using conductive biopolymers are limited owing to insufficient printability and lack of effective cross-linking strategy. To some extent, the 3D printable conductive polymers are nearly insoluble in water, exhibited poor bioactivity, and less degradability owing to the high crosslinking degree [26]. A study by Spencer et al. reported the use of gelatin/PEDOT: PSS based conductive hydrogels with controlled biodegradability (~60% up to 56 days) and excellent survivability (viability ~92%) of C2C12 myofibroblasts [26]. In another studies, various bioprinted conductive hydrogels were fabricated for encapsulating kidney (viability ~90%), neuron (viability ~50–60%), and cardiomyocytes cells (viability ~80–90%) and displayed moderate or good electrical conductivity without any proper

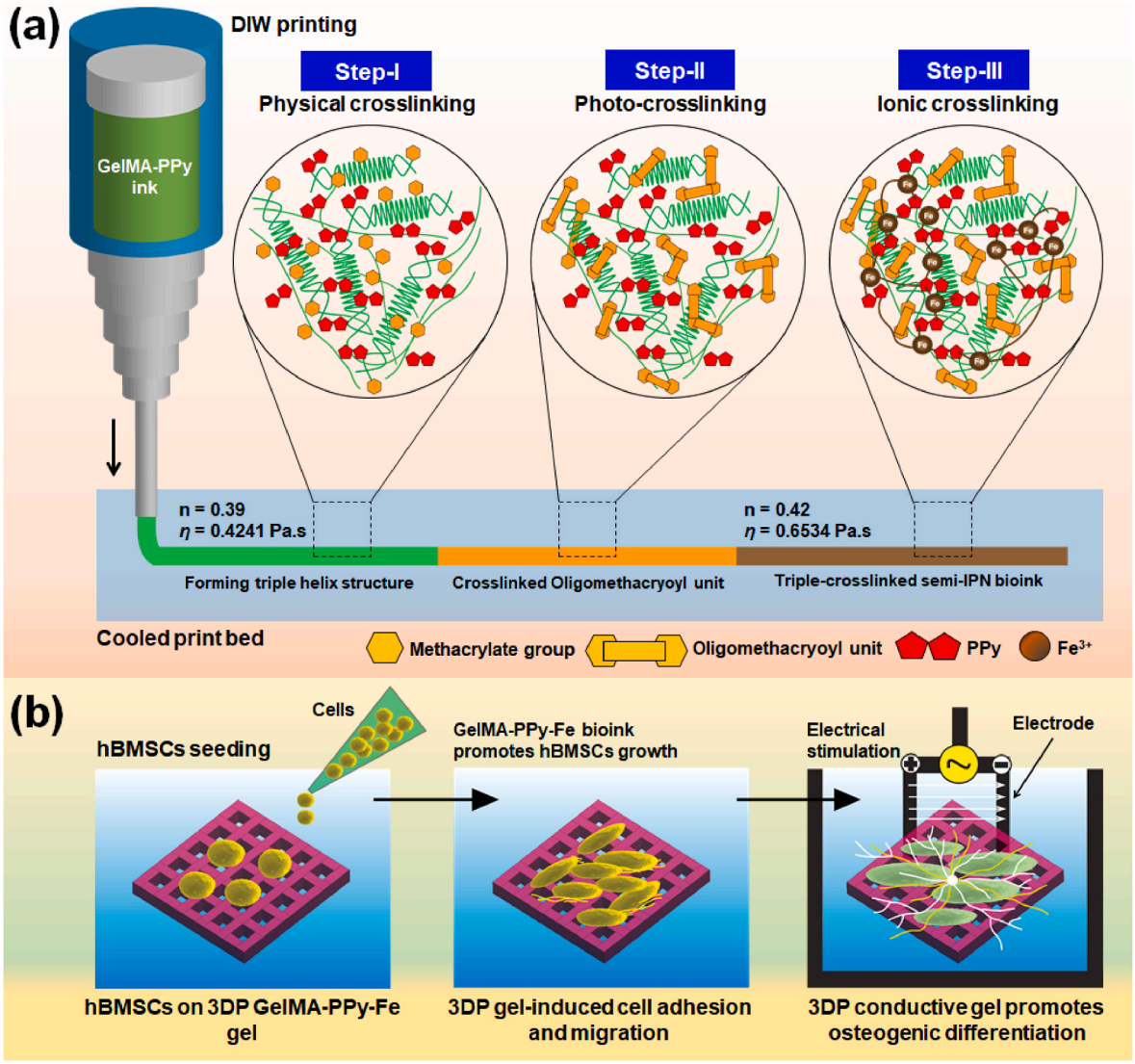

Scheme 1. (a) Schematic illustration for the fabrication process of 3D printed triple-crosslinked (thermo-photo-ionic crosslinking) GelMA-PPy based hydrogel for improving the conductivity and bioactivity. **(b)** An overview of direct current stimulation for regulating stem cell proliferation and osteogenic differentiation. The n and η represents the shear-thinning index and apparent viscosities of the GelMA and GelMA-PPy-Fe bioink, respectively.

evidence of electrical stimulation system [27–29]. Therefore, integrating all the above-mentioned features into a single hydrogel is highly desirable for successful demonstration of electric field-guided cell proliferation and differentiation. A comparative table of various 3D printable and bioprintable conductive hydrogels used in tissue engineering application is given in Table S1.

Considering the fact that an ideal conductive hydrogel ink must have excellent printability with higher mechanical property and biocompatibility, we propose a one-step *in situ* biofabrication of a conductive bioink using PPy-grafted gelatin methacryloyl (GelMA-PPy) with a novel cross-linking strategy. The formulated bioink exhibits high-performance 3D printability with a dynamic semi-IPN network. The 3D printed GelMA-PPy hydrogel is electrically active and tested for continuous microcurrent stimulation (EFs) of human mesenchymal stem cells (hBMSCs) to accelerate osteogenesis. The as-prepared bioink was triple-cross-linkable (physical, ultraviolet, and ionic cross-linking), mechanically robust, and displayed excellent electrical conductivity even after 3D printing. hBMSCs biocompatibility in the presence of conductive 3D printed GelMA-PPy scaffolds was investigated using a proliferation assay, morphometric study, quantitative real-time polymerase chain reaction, western blotting, and RNA sequencing analysis. We observed an improvement in the osteogenic potential of hBMSCs grown on GelMA-PPy scaffolds with 250 mV EF stimulation. Scheme 1 depicts an overview of the 3D printable bioink preparation, cross-linking mechanism, and 3D electrical stimulation of hBMSCs using the GelMA-PPy-Fe hydrogel. In addition, the behavior of hBMSCs in the presence of varying EFs was investigated to determine the biocompatibility of microcurrent stimulation for bone tissue engineering applications.

1. Experimental section

1.1. Materials

Gelatin (type A, gel strength: 300 bloom) and pyrrole (Py, purity: 98%), and methacrylic anhydride (94%) were purchased from Sigma-Aldrich, USA. Iron (III) chloride hexahydrate (purity: 99%) was obtained from Fischer Chemicals Co., Thermo Scientific, USA. A custom-designed microcurrent stimulation device was obtained from Lee-Chun Electronics Ltd., Republic of Korea. A fully automated 3D bioprinter was purchased from Cellink Corporation, Sweden. The human bone-derived mesenchymal stem cells (hBMSCs) were supplied by the Korean Cell Line Bank, Seoul National University, Republic of Korea. The RNAzol, Live-dead staining kit, F-actin probe was purchased from Sigma-Aldrich, USA. The WST-1 cell viability assay kit was obtained from DoGen Bio, Republic of Korea. The PrimerScript™ RT kit and SYBR green qRT-PCR master mix were purchased from the TaKaRa Bioscience, Japan. The Western blot antibodies and cell culture reagents were purchased from the Welgene, Republic of Korea and Santa Cruz Biotechnology, USA.

1.2. Synthesis and characterization of GelMA

GelMA foam was synthesized following previous reports [30–32]. Briefly, 10 g of Type A gelatin (Sigma-Aldrich, USA) was dissolved in 100 mL sterile PBS (pH 7.4), followed by the addition of 2 mL of methacrylic anhydride (Sigma-Aldrich, USA) with continuous stirring at 40–45 °C for 2 h. After 2 h, the reaction was stopped by adding 2-fold warm PBS and stirred for 10 min. The resulting solution was dialyzed against sterile distilled water using a dialysis tube (12–14 kDa cutoff molecular weight) for 5–7 days to remove the methacrylic acid. Next, the GelMA solution was concentrated and lyophilized for 7 days to obtain a white foam and stored at −80 °C until use. The lyophilized GelMA was characterized by FT-IR to study the methacrylation. The as-obtained GelMA (50 mg in D_2O) was characterized by the ^1H NMR using a Bruker NMR (600 MHz). For analyzing the degree of substitution (DS), the spectra were normalized to the Phenylalanine signal (δ = 7.2–7.4 ppm) of gelatin and then integrated into the vinyl proton (δ = 5.4–5.6) of both gelatin and GelMA. The DS of GelMA was calculated according to **Eq. (1)**:

$$DS = \left(1 - \frac{A_H(5.4\ \&\ 5.6)\ \text{of GelMA}}{A_H\ (5.4\ \&5.6)\ \text{of Gelatin}}\right) \times 100\%$$

1.3. Synthesis and characterization of PPy-grafted GelMA

The Py grafted GelMA was synthesized as reported previously [33]. Briefly, 1 g of GelMA was dissolved in PBS at 45–50 °C, followed by the addition of excess Py (400 μL) and magnetically stirred for 2 h. After that, 0.1 g of APS was slowly added to the reaction mixture and stirred overnight, keeping the heat around 40 °C. APS reacted with the Py and grafted *in situ via* reacting with lysine proton of GelMA at the methacrylation point and polymerized to form PPy. After synthesizing, the GelMA-PPy solution was dialyzed in D.W. for 2–3 days to remove the excess and unreacted APS. Finally, the resulting solution was lyophilized to obtain the pure GelMA-PPy foam. The as-synthesized material was kept at −20 °C until further use. FT-IR and ^1H NMR were used to characterize the PPy-grafted GelMA.

1.4. Preparation of GelMA-PPy based conductive hydrogel

For hydrogel preparation, 15 wt% of GelMA-PPy was dissolved in sterile DW at 40 °C under mild stirring. After that, 0.25% of lithium phenyl-2,4,6-trimethylbenzoylphosphinate (LAP) was added to the solution and additionally stirred for 30 min. After complete dissolution of the LAP, the hydrogels were irradiated with 365 nm UV light (5 W cm^{-2}, Skycare UV Electronics, Republic of Korea) for 30–35 s, followed by the addition of 0.2 M $FeCl_3$ solution. The as-prepared hydrogel was termed as GelMA-PPy-Fe, respectively. The hydrogels devoid of PPy (only 15 wt % GelMA) with Fe (= GelMA-Fe) were taken as control hydrogels.

1.5. Characterization of GelMA-PPy hydrogel

Field emission scanning electron microscope (FE-SEM, Hitachi S4800, USA) was used to observe the freeze-dried morphology of the 3D printed hydrogel scaffolds using an accelerating voltage at 10 kV. The porosity and pore diameter of the hydrogel scaffold was measured using ImageJ software (v1.8, NIH, Bethesda, USA). Three independent images were analyzed to calculate the scaffold porosity. The conductivity of the developed hydrogels (2.5 × 1 × 0.2 cm) was measured in terms of resistance (R) using a digital multimeter (FLUKE, 17 B+, WA, USA). The resistivity (ρ) of the GelMA-PPy-Fe hydrogel (both gel and 3D printed) was calculated using **Eq. (2)** as reported earlier [6]:

$$\rho = \mathrm{R}\frac{A}{L} = \mathrm{R}\frac{W \times H}{L}$$

Where A is the hydrogel's cross-sectional area, L indicates the length, and W and H represent the width and height of the hydrogel, respectively. Therefore, the electrical conductivity (σ) was calculated by using **Eq. (3)**:

$$\sigma = \frac{1}{\rho}$$

Where σ represents the electrical conductivity of the hydrogel/printed gel in milisimens per meter (mS cm^{-1}), respectively. The swelling efficiency of the developed hydrogels was evaluated as reported in our previous study [3]. The % of swelling efficiency of the developed hydrogel scaffolds was determined using the following **Eq. (4)**:

$$\%\ swelling = \frac{W_s - W_d}{W_s} \times 100$$

Where, W_s and W_d are the weight of the scaffolds after and before

soaking in PBS. The viscoelastic property of the GelMA-PPy hydrogel was measured by a rotational rheometer (ARES G2, TA Instruments, USA) at varying frequency (0.1–100 Rad s^{-1}) and shear rate (0.1–100 s^{-1}) with a 1% strain rate. The hydrogels' modulus was also examined using temperature ramp test (4–35 °C). The thixotropic measurements were conducted up to 600 s with initial 0.1 s^{-1}, followed by high shear rate (1000 s^{-1}), and low shear rate (0.1 s^{-1}), respectively. The tensile and compressive strength of the as-prepared hydrogel was measured using a universal tensile machine (A&D Digital, Japan) at room temperature. The wettability measurements were taken at room temperature using a contact angle measurement device (Phoenix MTT, SEO, Republic of Korea).

1.6. 3D printing of conductive GelMA-PPy hydrogels

1.6.1. Preparation of the conductive bioink

For 3D printing, the GelMA-PPy (15 wt%) and LAP (0.25%) were dissolved in 1 × PBS at 37 °C overnight. After that, the liquid gel solution was injected into the printing cartridge (6.5 × 1 cm) and kept at 4 °C until further use. The physical crosslinking of gelatin occurred at low temperatures, which is beneficial for 3D printing using a low-temperature print bed. The GelMA was used as a control sample for 3D printing respectively.

1.6.2. CAD modeling and 3D printing

The target models were designed in Solidworks software (Dassault Biosystems, USA) and exported as STL files, sliced by Slicr3r v1.3.0 open-source software finally converted into a G-code printer file. A Cellink BioX (Cellink Corporation, Sweden) 3D bioprinted was utilized for 3D printing of GelMA-PPy hydrogels. The 15 wt% GelMA-PPy was chilled at 4 °C for at least 5–6 h and printed on a pre-chilled printer bed (temperature: 4–10 °C) using the same printer setting. A conical plastic head printing nozzle with a diameter of 400 μm (=22G) was used to print all the constructs. The printing parameters are listed in Table S2. After 3D printing, all the constructs were UV cured for 30 s, followed by incubation in a 0.2 M $FeCl_3$ bath for 5–10 min, and finally washed several times with PBS to remove the unreacted polymer and Fe^{3+} ions.

1.6.3. Printability and critical nozzle height calculation

The printability parameters were evaluated for GelMA-PPy hydrogels as described in our previous study [3,8,34]. Briefly, a single layer of a 20 × 20 × 1 mm construct was carefully printed and crosslinked immediately with varying printing speeds (2–8 mm s^{-1}). Then, each of the printed strands was photographed using an inverted optical microscope to measure the printed strand width to measure the strand uniformity (*U*) and printability factor (*Pr*), respectively. To highlight the influence of printing speed on the cross-sectional area of the construct, the flow rate was normalized to the printing speed in terms of volume conversion relationship [35] using **Eq. (4)**:

$$\frac{A_P}{A_N} = \frac{U_N}{U_P}$$

Where U_P is the printing speed of the printer, inversely proportional to the linear velocity at the nozzle exit point denoted as U_N. Therefore, U_N is directly connected to the filament formation, which is equal to the cross-sectional area (A_N) of the filament, where no ink spreading or stretching, or clogging occurs. Therefore, for a given printing speed with a fixed pressure, there will be a linear correlation ($y = mx + c$, $R^2 = 0.999$) between printing speed and extrusion rate, respectively. The critical nozzle height (H_c) was calculated as reported previously using **Eq. (5)**:

$$H_c = \frac{V_d}{V_n \times D_n}$$

Where V_d is the volume of the hydrogel extruded per unit time (denoted as extrusion rate $cm^3\ s^{-1}$), V_n is the nozzle moving speed with respect to the printing base (denoted as printing speed), and D_n is the nozzle diameter (= 400 μm), respectively.

To evaluate the printability of the developed hydrogels, a full-thickness rat bone model was designed using Solidworks software and exported to the STL file. The first layer height was adjusted to 0.25 mm to support the upper layers. The 3D printing was conducted using a Cellink BioX printer with pre-determined parameters, and the printing time was measured about 15 min, respectively. After 3D printing, the printed construct was immediately crosslinked as mentioned before and photographed. After that, a digital image processing software (ImageJ, v1.8, NIH, Bethesda, USA) was used to evaluate the surface property of the printed bone model.

1.7. Electrochemical measurements

For electrochemical measurements, cyclic voltammetry (CV) was conducted using three electrode setup with a working electrode, a reference electrode (Ag/AgCl), and a counter electrode (Pt). The glassy carbon electrode (GCE) was used as working electrode for coating the hydrogel solution. For this, the GCE was polished with diamond-alumina paste and sonicated in a mixture of ethanol/acetone (1:1 ratio) for 15 min. After that, the GCE was washed with sterile DI water and dried before hydrogel coating. Next, 25–30 μL of hydrogel solution was drop casted on to the surface of the GCE in the presence of Nafion (ionic conductivity ~ $1.23 \times 10^{-2}\ \Omega^{-1}\ cm^{-1}$) and dried properly before CV measurement. After that, the GCE/GelMA-PPy-Fe electrode was applied with definite potential and the electrode oxidation started as soon as the current began to flow. The electrochemical impedance was conducted by mean of Nyquist plot using the electrochemical impedance spectroscopy (EIS).

1.8. 3D bioprinting, cytotoxicity, and in vitro osteogenic differentiation

The hBMSCs (passage-3) were maintained in DMEM, supplemented with 10% FBS, and 1% antibiotics in a humidified atmosphere at 37 °C with 5% CO_2. The cell culture was conducted in two different ways: (1) the conventional 2D cell culture (surface cell seeding) and (2) hBMSCs-laden GelMA-PPy culture (3D bioprinting). The detailed experimental protocol is as following.

1.8.1. 3D bioprinting and cell cytotoxicity evaluation

Prior to 3D bioprinting, the 15 wt% GelMA-PPy was UV sterilized and incubated in serum-free DMEM media at 37 °C until fully dissolved. After that, 0.25% LAP photoinitiator was mixed with the GelMA-PPy solution. Next, 500 μL of hBMSCs suspension was mixed with the GelMA-PPy solution to achieve a final hBMSC concentration of 5×10^4/3 mL of GelMA-PPy. After that, the bioink was carefully loaded onto a 5 mL plastic printing cartridge and incubated at 4 °C for 10 min to initiate gelation. Next, the bioink was carefully printed onto a cooled platform using a 6-well plate, and crosslinked using a UV module (365 nm) equipped with the bioprinter. The construct dimension was 1 × 1 × 0.5 cm, respectively. The extrusion pressure and printing speed was maintained at 50 ± 2 kPa and 5 mm s^{-1} throughout the bioprinting process. After UV crosslinking, the bioprinted construct were carefully detached from the well plate and immersed into a solution of 0.05 M $FeCl_3$ for 3 min. The ionic crosslinking for bioprinting was chosen *via* using various $FeCl_3$ concentration (0.05, 0.1, 0.25, and 0.5 M) and its impact on viability. We found maximum cell viability (~95% after 24 h) using 0.05 M $FeCl_3$ crosslinking and thus judiciously chosen for bioprinting study. For the conventional 2D culture, the same 3D printing process was conducted without hBMSCs.

The cytotoxicity of the hBMSCs was assessed using WST-8 assay and Live/Dead assay with or without EFs treatment. For this, both the 2D and 3D culture system received a daily basis of EFs stimulation (100, 250, and 500 mV/20 min/day) up to 3 days. Besides, the optimum EFs

dose was also tested *via* incubating the hBMSCs without any hydrogel but in the presence of EFs. To find the optimum dose of EFs, hBMSCs (2.5×10^4 cells/2 mL/6-well) were seeded in a 6-well plate and stimulated with EFs. After desired time points, the cells were incubated with 500 μL of WST-8 dye and the viability was measured spectrometrically. Based on the initial screening, we found 250 mV EF stimulation as an effective dose for hBMSCs proliferation. Moreover, the biocompatibility of the hBMSCs in the presence GelMA and GelMA-PPy-Fe hydrogel was also assessed after 3 days of incubation using WST-8 assay. For Live/Dead assay, the 2D and 3D culture cells (4×10^4 cells/2 mL/6-well) were incubated with 10 μL of acridine orange/propidium iodide dye (1 mg mL^{-1}, 1:1 ratio each) solution and incubated for 15 min at 37 °C. After that, the cells were washed with PBS and photographed using an inverted FL microscope. The number of Live/Dead cells were quantified using ImageJ software (v1.8, NIH, USA) equipped with Live Cell Counter tool.

1.8.2. Evaluation of cytoskeleton morphology

The cytoskeletal morphology of the hBMSCs in the presence of EFs stimulation was assessed after 5 days of incubation. For this, 2.5×10^4 cells were seeded onto the printed hydrogels 9GelMA and GelMA-PPy-Fe) and incubated for 24 h. After that, the cells were exposed to EFs (250 mV/20 min) for a daily basis up to 5 days. After desired time period, the cells were fixed with 4% paraformaldehyde, followed by permeabilization with 0.1% Triton-X 100. After that, the cells were blocked with 1% BSA solution for 1 h. Next, the cells were washed with PBS and incubated with 200 μL of Rhodamine conjugated F-actin probe (AAT Bioquest, CA, USA) for 1 h. After actin staining, the cells were washed twice with PBS and stained with 500 μL of DAPI solution to stain the nucleus. After desired staining and incubation, the cells with printed hydrogel was immersed in 1 mL PBS and visualized using an inverted fluorescence microscope (DMi8, Leica, Germany) with proper filter cubes. The image analysis was carried out using ImageJ Fiji software (NIH, Bethesda, USA). The actin alignment (anisotropy) was determined using the Cell Directionality and OrientationJ tool with JavaScript commands. The nuclear aspect ratio (width/length) was measured by measuring the length and width of the nucleus. The image analysis was carried out using 5 independent images with at least 10 cells/field.

1.8.3. In vitro mineral indication study

For osteogenic differentiation study, the 2D (cells seeded onto the hydrogel surface) and 3D (3D bioprinted) culture cells (4×10^4 cells/1 mL/24-well) were additionally grown in osteogenic differentiation media (Gibco-BRL, Grand Island, USA) for up to 14 days. The alizarin Red-S (Sigma-Aldrich, USA) staining was conducted to examine the mineralized nodule formation after 14 days of incubation. After ARS staining, the mineralized nodule formation was photographed using an inverted optical microscope (Zeiss, Germany). For the bioprinted construct, cross-sectional morphology was also examined to observe the cell infiltration and mineralization. To evaluate the osteoblastic gene and protein markers expression in the presence or absence of EFs stimulation, real-time polymerase chain reaction (qRT-PCR), western blotting (WB), and immunocytochemical (ICC) assay was performed.

1.9. Macrophage polarization and osteo-immunomodulation study

The immunopolarization potential of fabricated hydrogel scaffolds was investigated through fluorescent activated cell sorting (FACS), morphometric observation, immunocytochemical (ICC) staining, and real-time PCR (qRT-PCR) analysis. Mouse monocyte (Raw 264.7) cells were used in this study. The methods are as follows.

1.9.1. Flow cytometry

For FACS analysis, the Raw 264.7 cells (4×10^4 cells/2 mL/6-well plate) were seeded onto the 3D printed hydrogels and incubated for 24 h. After that, the cells were harvested using 0.25% Trypsin-EDTA (Gibco-BRL, USA) and centrifuged to pellet down the cells. Next, the cell suspension was fixed with 4% paraformaldehyde for 5 min and permeabilized by 0.1% Triton-X 100, followed by incubation with F_c receptor blocker (AAT Bioquest, CA, USA) for 10 min. After blocking, the cells were incubated with primary antibodies against NOS2 (sc-7271, SCBT, USA, M1 marker, SCBT, USA, 1:500) and CD163 (sc-33715, M2 marker, SCBT, USA, 1:500), followed by incubation with fluorescent secondary antibodies (*m*-IgG kappa BP-FITC, sc-516,140, SCBT, USA, 1:500) for 1 h. After that, the cells were rinsed with PBS twice and re-suspended in 1 mL of PBS for flow cytometry analysis. The cells were sorted using 488 nm excitation laser and populations were gated to M1 to find the percentage of NOS2 and CD163-positive cells.

1.9.2. Immunocytochemistry

For immunocytochemical (ICC) staining, the Raw 264.7 cells (4×10^4 cells) were fixed with 3.7% PFA solution and permeabilized using 0.1% Triton-X 100 for 5 min. After that, the cells were blocked using 1% BSA (Sigma-Aldrich, USA) solution for 1 h. Next, the blocked cells were incubated with primary antibodies against NOS2 (1:250) and CD163 (1:200), followed by incubation with fluorescent secondary antibodies (1:250). After desired staining, the cells were incubated with 10 μL of DAPI to stain the nucleus. After complete staining, the cells were mounted with appropriate mounting medium and visualized using an inverted fluorescence microscope with 40 × objective lens. The images were captured using appropriate filters and processed with ImageJ software (v1.8, NIH, Bethesda, USA).

1.9.3. qRT-PCR analysis

The qRT-PCR was performed to verify the activation of pro-inflammatory (*TNFα* and *IL-1β*) and anti-inflammatory (*IL-4* and *IL-10*) gene markers with or without scaffolds. The qRT-PCR was performed as reported in our pervious study. Briefly, the total RNA was isolated using RNAzol reagent (Sigma-Aldrich, USA) and the cDNA synthesis was carried out using the cDNA synthesis kit (RevertAid First Strand cDNA synthesis Kit, Thermo-Fischer Scientific, USA) as per manufacturers guidelines. A CFX96 Maestro real-time PCR system (Bio-Rad, USA) was used to perform the qRT-PCR experiment using β-actin as a loading control. The specified primer sequences used for qRT-PCR analysis is listed in Table S3.

1.9.4. Osteo-immunomodulation study

For this, the Raw 264.7 monocyte cells (4×10^4/6 well plate) were seeded onto the printed hydrogels and cultured in DMEM media for 24 h. After that, the macrophage/monocyte culture media was collected and centrifuged at 3000 rpm to remove the debris. The culture media soup was considered as macrophage conditioned media. The pure GelMA hydrogel and GelMA-PPy-Fe hydrogel were considered as control and treated group (M-CM), respectively. To investigate the effect of M-CM on osteogenesis, the hBMSCs were cultured w/or w/o M-CM for 7 and 14 days. After that, mineralized nodule formation and ALP activity was assessed using ARS staining and ALP colorimetric assay kit (AAT Bioquest, CA, USA).

1.10. Transcriptome analysis

The transcriptome analysis was carried out to evaluate the differentially expressed genes (DEGs) in various experimental groups after 7 days of treatment. The experimental groups include the control group w/o EFs, 2D culture group w/EFs, and 3D culture group w/EFs, respectively. For this, the total RNA was harvested after 7 days of osteogenic differentiation by RNAzol (Sigma-Aldrich, USA) reagent and used to prepared the standard RNA library. The QuantiSeq 3′ mRNA-Seq was performed using a next generation RNA sequencer (Nova-Seq 6000, PE100 bp, CA, USA) using the reference genome hg19 and genome database UCSC for human. The raw data was processed using the ExDEGA graphic software (ebiogen, Republic of Korea) and normalized

to log2 (average of normalized data in each group) and statistical analysis was carried out using Student's *t*-test. Additionally, the gene set enrichment analysis (GSEA) and gene ontology (GO) analysis was carried out using web-based bioinformatics tools (DAVID and GSEA) to evaluate the PPI enrichments in various biological pathways. The genes (Up/Down-regulated) with a fold change of ≥2.0 and a *P* value < 0.05 were considered as statistically significant. Finally, STRING software (https://string-db.org/) was used to evaluate the possible interaction and co-expressed gene and/or protein networks.

1.11. Statistical analysis

The statistical analysis was carried out using Origin Pro software (v9.0, Origin Labs, USA). A One-way analysis of variance (ANOVA) and Student *t*-test was carried out to verify the significant different between control and treatment groups. Statistical significance was set at $^{*}p < 0.05$, $^{**}p < 0.01$, and $^{***}p < 0.001$. Data are reported as mean ± s.d. of triplicate ($n = 3$) experiments.

2. Result and discussion

2.1. Characterization of the GelMA-PPy hydrogel ink

We obtained the highly pure and foam-like GelMA and GelMA-PPy (Fig. S1a) with a degree of substitution (DS) value of 71.44 ± 0.32% and 22.54 ± 0.28%, respectively, as predicted by ^{1}H NMR measurements. The Fourier transform-infrared spectra (FT-IR) of GelMA and GelMA-PPy exhibited characteristic peaks at 3308–3287 cm^{-1}, corresponding to the–O–H stretching vibrations of gelatin. Additional peak at 1451 cm^{-1} were assigned to the methacrylated –CH_2 of GelMA and GelMA-PPy, which were slightly shifted to 1438 cm^{-1}, indicating the unmethacrylated amino acid moities (Fig. S1b). Moreover, the peak at

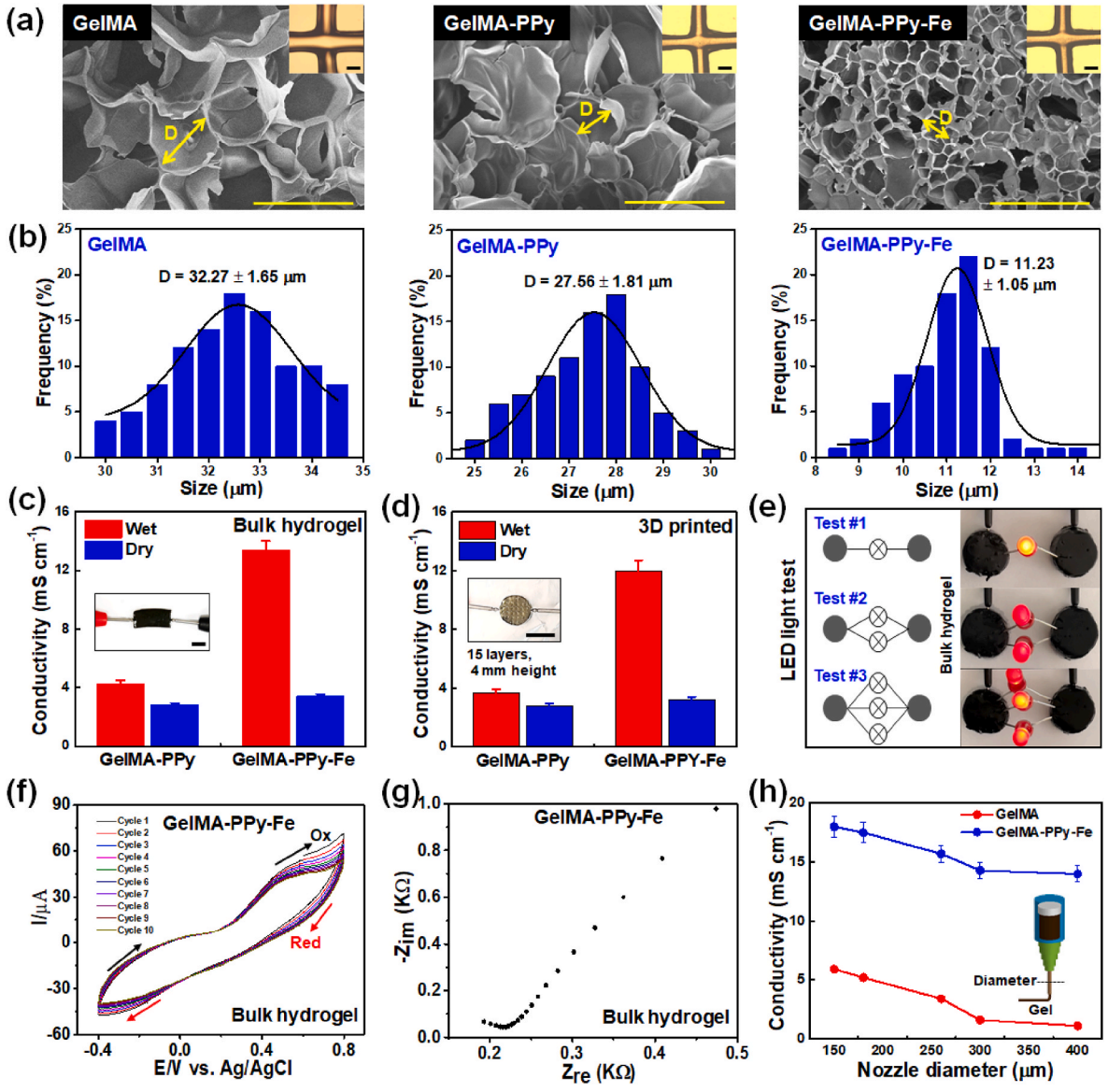

Fig. 1. **(a)** FE-SEM images of the freeze-dried GelMA, GelMA-PPy, and GelMA-PPy-Fe hydrogel scaffolds. Insets are optical micrographs of the corresponding hydrogels. Yellow arrow indicates the pore diameter of corresponding images. Scale bar: 50 and 100 μm **(b)** Pore size distribution of the fabricated scaffolds. **(c)** Digital photographs of the designed hydrogels with fixed dimensions used for conductivity test. Scale bar: 10 mm. **(d)** Conductivity of the GelMA-PPy and GelMA-PPy-Fe hydrogels in wet and dry form. **(e)** Conductivity test of the 3D printed GelMA-PPy and GelMA-PPy-Fe hydrogels. **(f)** Cyclic voltammetry measurement of the GelMA-PPy-Fe hydrogels indicating electrical redox activity. **(g)** Measurement of electrochemical impedance of GelMA-PPy-Fe hydrogels using Nyquist plot. **(h)** Effect of nozzle diameter on filament conductivity of the GelMA and GelMA-PPy-Fe hydrogel ink. (For interpretation of the references to color in this figure legend, the reader is referred to the Web version of this article.)

around 1240 cm^{-1} in gelatin was shifted to the higher wevenumber in case of GelMA (1245 cm^{-1}) and GelMA-PPy (1242 cm^{-1}), indicting the presence of $–CH_2$ of the methacrylated protons. To confirm the structural changes, ^1H NMR spectra were recorded. PPy specifically reacts with the double bond of the methacrylated proton [2H], presenting lysine (Lys) and histidine (His) residue of GelMA. The ^1H NMR spectra of GelMA exhibited characteristic resonance signals at $\delta = 5.4$ and 5.6 ppm (black arrow), corresponds to the vinyl protons (H_a and H_b) of the methacryloyl groups [2H] present in Lys and His residue of gelatin, indicating the typical amidation reaction (Fig. S2), which was absent in pure gelatin [30]. Moreover, a predominant signal at $\delta = 7.3–7.4$ ppm (dotted red arrow) and $\delta = 0.8$ ppm (dotted green arrow) were attributed to the presence of unmethacrylated aromatic protons [5H] of phenylalanine (Phe) and methyl protons [3H] of valine (Val), leucine (Leu), and isoleucine (Ile) of the gelatin backbone. Interestingly, the intensity of the two vinyl proton [2H] peaks at 5.4 and 5.6 ppm (red arrow) of GelMA was reduced due to breakage of double bonds and introduction of a single bond with PPy. These results indicate the successful grafting of PPy onto the GelMA chain by reaction with double bonds.

Both GelMA (15 wt%) and GelMA-PPy (15 wt%) were dissolved in an aqueous solution and exposed to the 365 nm UV light (5 W cm^{-2}) for 30 s. After UV cross-linking, the gels were transferred into a 0.8 M $FeCl_3$ bath for 5 min. UV cross-linking yields double oligomethcryoyl units, and Fe^{3+} cross-linking ionically joins the –COOH of GelMA with grafted PPy. Ionic cross-linking made the hydrogels tougher than UV cross-linking. To understand the effects of dual cross-linking, we observed the scanning electron microscopy (SEM) morphology of the freeze-dried GelMA, GelMA-PPy, and GelMA-PPy-Fe scaffolds; the results are shown in Fig. 1. Notably, the Fe^{3+} cross-linking drastically reduced the porosity of the scaffolds starting from 32.27 ± 1.65 μm (GelMA) to 27.56 ± 1.81 μm (GelMA-PPy) to 11.23 ± 1.05 μm (GelMA-PPy-Fe) as indicated in Fig. 1 (a, b). The smaller pores (<50 μm) usually results in greater osteogenic differentiation of bone cells than proliferation owing to the hypoxic environment and behaves like a stiff matrix. Thus, bioprinted hydrogels with smaller porosity may decrease the nutrient and oxygen uptake, while indicung the hypoxia-mediated angiogenesis and osteogenic capabilities [36]. Trabecular bone (spongy bone) has greater porosity (≈90%) than cortical bone (≈20%), meaning that cortical bone is highly dense and compact sutucture. In this context, the GelMA-PPy-Fe scaffold with microporosity are more likely suitable for inducing osteogensis *via* adsorpbing bone-indicng porteins and ion-exchange [37,38]. As the Py added to the GelMA in excess, the addition of PPy onto GelMA further increased the DS% of GelMA. Thus, ionic cross-linking made the hydrogels more tightly connected to the internal networks owing to the presence of more PPy groups, decreasing the porosity of GelMA-PPy-Fe scaffolds. Hence, the triple-cross-linking strategy yields tougher hydrogels with smaller pororsity than conventional GelMA scaffold and can be used as a long-term implantable biomaterial for bone tissue engineering applications.

2.2. Conductivity, viscoelasticity, and printability of the GelMA-PPy ink

Biocompatible hydrogels with tunable conductivity are essential for the electrical stimulation of stem cells [39,40]. Although PPy incorporation into the polymer matrix enhances conductivity, crystallinity, and charge-carrier mobility, it also acts as a dopant owing to its excellent anionic properties [23,33,41]. The resistivity (Ω) of the hydrogels was measured using a digital multimeter. Digital photographs of the prepared hydrogel with specific dimensions are shown in Fig. 1 (c, d). As shown in Fig. 1c, the conductivity of GelMA-PPy-Fe (~13.5 mS cm^{-1}) was higher than that of GelMA-PPy (~4.2 mS cm^{-1}) in gel form. This was due to the superior cross-linking of the PPy network with Fe^{3+} ions, resulting in a continuous electron flow. Moreover, we also calculated the pKa value to determine the conductive nature of the GelMA-PPy-Fe hydrogel and the results are shown in Fig. S3. It is interesting to note that the PPy is sensitive to the pH of the buffer solution. At acidic pH the PPy chain is protonated with a less pKa value and remains conductive. However, at basic pH the PPy deprotonated with a pKa value of 8.21, which makes it a little less conductive. This is due to the change in the electronic configuration of the quinoid structure of PPy and intercalation of the adjacent anions. The pKa value of GelMA-PPy-Fe at pH 7.4 is calculated to be 7.13. It is well known that pKa value is inversely proportional to the conductivity of the material [42]. Therefore, it is assumed that pH 7.4 (mild basic) the grafted PPy will experience mild deprotonation and therefore, a slight decrease in conductivity. The conductivity of the GelMA-PPy-Fe after incubating 7 days in PBS media (pH 7.4) is calculated to be 9.6 ± 1.3 mS cm^{-1}, respectively. The decreased conductivity is also due to the less availability of the anions as the PPy chains and –COOH chains of GelMA are crosslinked with Fe^{3+} ions (base-ligand chelation). We designed a 20 × 20 mm construct using the direct ink writing (DIW) method to test the conductivity in the printed form. Notably, the conductivity of GelMA-PPy-Fe (~12.8 mS cm^{-1}) remained nearly the same even after 3D printing, and the introduction of Fe^{3+} ions into the GelMA-PPy network significantly improved the conductivity (Fig. 1d). Such a unique conductivity of GelMA-PPy-Fe is close to the conductivity of the human cortical (~0.2 mS cm^{-1}) and cancellous bone (~0.79 mS cm^{-1}) [43]. Therefore, we anticipated that the fabricated 3D hydrogel would be safe for bone tissue engineering applications. However, in the dry form, the conductivity decreased owing to the porous structure and decreased electron flow through the scaffolds. The superior conductivity of the GelMA-PPy-Fe hydrogel was also investigated using a light-emitting diode (LED) test. As shown in Fig. 1e, the LED was fully illuminated when the hydrogel was connected to an external power supply, indicating the conductive nature of the developed hydrogel. Cyclic voltammograms and electrochemical impedance of the GelMA-PPy-Fe hydrogels were obtained using a three-electrode system to evaluate their electrochemical performance. As demonstrated in Fig. 1f, the GelMA-PPy-Fe exhibited a broad anodic peak around 0.49 V (oxidation) and cathodic peak at approximately −0.36 V (reduction), with $E_{1/2}$ (half-wave potential) at around 0.256 ± 0.04 V, nearly consistent up to 10 cycles. Therefore, the ionic cross-linking of GelMA-PPy significantly changed the electrical conductivity, which is consistent with previous reports on conductive alginate and alginate-gelatin-based hydrogels [23,44]. Notably, the cyclic voltammogram was consistent with that obtained from the Nyquist plot (Fig. 1g), indicating the low resistivity of the GelMA-PPy-Fe hydrogel [45–47]. The Nyquist plot exhibited a nearly compressed semicircle with a low charge transfer resistance (~0.12 Ω) for GelMA-PPy-Fe hydrogels, similar to previous reports [48]. We also observed a negligible change in the conductivity of the GelMA-PPy-Fe bioink printed with nozzles of varying diameters. However, the pure GelMA bioink exhibited a drastic change in conductivity with varying filament diameters (Fig. 1h).

A rotational rheometer was used to evaluate the rheological properties of the formulated biomaterial inks. We noticed that the hydrogels' shear moduli (G′ and G″) are temperature dependent (Fig. 2a). Both pure GelMA and GelMA-PPy-Fe hydrogels showed typical solid like behavior (G′ > G″) at low temperatures. The storage modulus of both the hydrogels reduced rapidly with increase in the temperature indicating temperature dependent shear thinning behavior. Moreover, both the hydrogels were observed to have a decreasing shear stress over increasing temperature further confirming their shear temperature dependent shear thinning behavior (Fig. 2b). The temperature dependent shear thinning property of the hydrogel shows that lower temperature is favorable for the 3D printing of the hydrogels. Next, we performed the frequency sweep test for the prepared hydrogels to determine the stability of the gel network. The hydrogels were thus subjected to a frequency sweep from 0.1 to 100 $Rads^{-1}$. Fig. 2c shows the logarithmic plot of the G′ (elastic modulus)/G″ (viscous modulus) versus various oscillatory frequencies for the GelMA and the GelMA-PPy-Fe hydrogels. The characteristic features observed at low changes

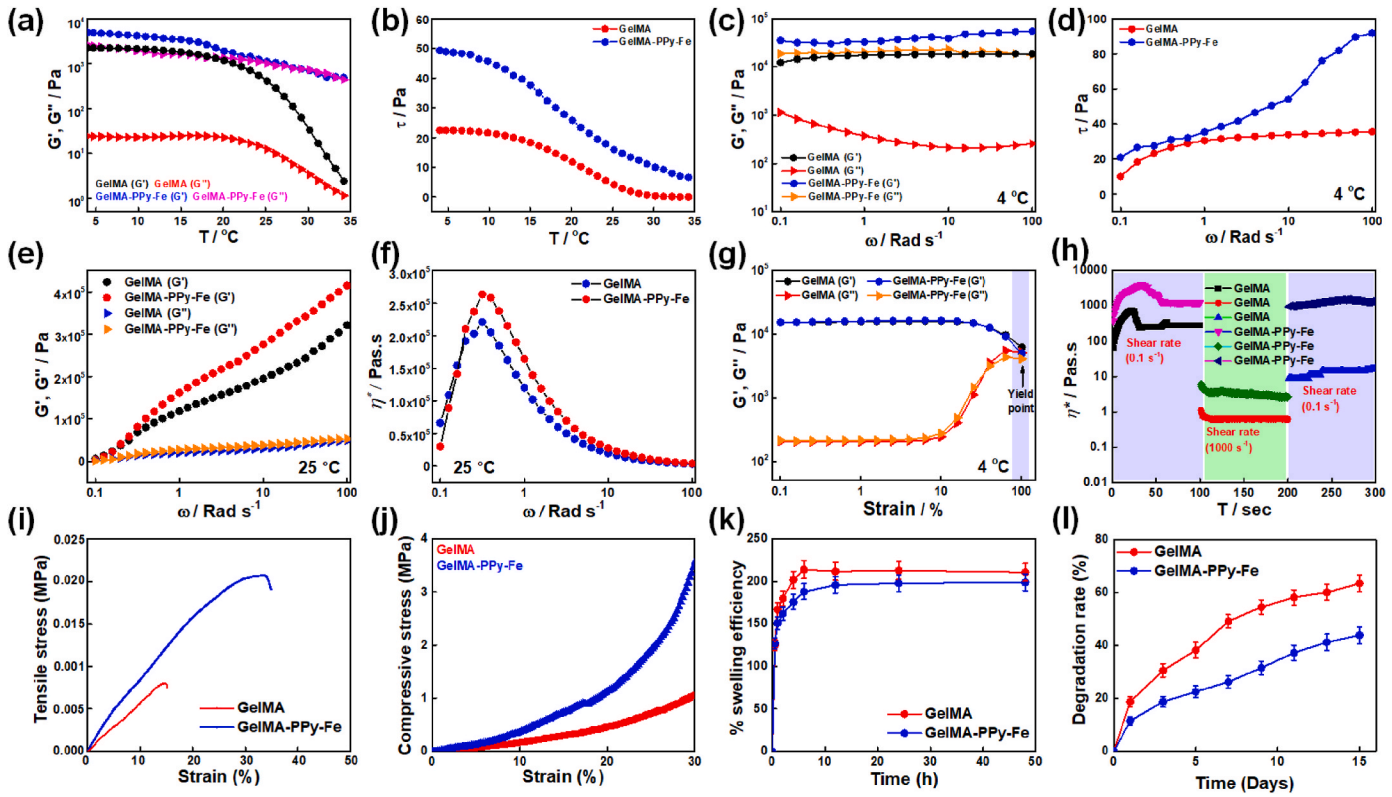

Fig. 2. Rheological measurements of the formulated bioink. **(a, b)** Representative shear moduli (G′ and G″) and shear stress (τ) of the GelMA and GelMA-PPy-Fe hydrogels under varying temperature (4–35 °C). **(c, d)** The frequency sweep test of the developed hydrogels at 4 °C. The frequency sweep test was conducted within 0.1–100 Rad s^{-1} range. **(e)** The frequency sweep test of the developed hydrogels at 25 °C. **(f)** The complex viscosity (η^*) measurement of the developed hydrogels at 25 °C. **(g)** Amplitude sweep test of the formulated hydrogels at 25 °C. The strain rate was 0.1–100%. **(h)** Thixotropic behavior of the developed hydrogels during continuous step-strain measurement within a shear range ($\dot{\gamma}$) of 0.1–1000 s^{-1}, indicating the recovery strength. **(i)** Tensile stress-strain curves of GelMA and GelMA-PPy-Fe hydrogels. **(j)** Uniaxial compressive strength and toughness of the fabricated hydrogel ink. **(k, l)** Swelling and degradation behavior of the developed hydrogel scaffolds in PBS at indicated time intervals.

of frequency shows the behavior at low changes of shear stress, while higher frwquencies display the features at high changes of stress. We observed a prominent platue in the GelMA-PPy-Fe hydrogel throughout the frequency range of 0.1–100 $Rads^{-1}$, indicating a highly stable crosslinked hydrogel. The only GelMA hydrogel failed to display a steady shear moduli with increase in the oscillatory frequency, indicating poor stability of the neat hydrogel. This behavior was further reflected in their charactristic shear stresses as a function of changing frequencies (Fig. 2d).

Next, we evaluated the viscoelastic nature of the formulated biomaterial inks within the frequency range of 0.1–100 Rad s^{-1}. As shown in Fig. 2e, at a high frequency (100 Rad s^{-1}), the storage modulus (G′) of the GelMA-PPy-Fe hydrogel increased to 414 × 10^3 Pa, which was much higher than that of the GelMA hydrogel (G′ = 321 × 10^3 Pa). At a low-frequency rate (0.1 Rad s^{-1}), the G′ for GelMA and GelMA-PPy were 6.21 × 10^3 Pa and 8.27 × 10^3 Pa, respectively. Similarly, the loss modulus (G″) of the GelMA and GelMA-PPy hydrogels at 100 Rad s^{-1} was found at 49.31 × 10^3 Pa and 53.02 × 10^3 Pa, respectively. Thus, the G″ and G' values for GelMA-PPy-Fe were enhanced owing to the high degree of cross-linking, resulting in a tougher and inner-connecting polymeric network after incorporating PPy and Fe^{3+} ions.

The gel underwent a critical sol–gel transition for a typical shear-thinning and shear-recoverable hydrogel. The hydrogel recovered immediately to its original shape as the shear stress was removed. The GelMA and GelMA-PPy hydrogel inks exhibited typical shear-thinning and yielding properties according to rheological measurements at 37 °C, which corresponds to the physiological temperature. As shown in Fig. 2f, the complex viscosity (η^*) of the developed hydrogel inks was measured at 1% strain, with a shear rate ranging between 0.1 and 100 Rad s^{-1}. The zero-shear viscosity (η) of the GelMA and GelMA-PPy were recorded as 74.31 × 10^3 Pa s and 88.24 × 10^3 Pa s, respectively. This was due to the high DS% of both GelMA and GelMA-PPy, and the ionic cross-linking of PPy with Fe^{3+} ions. As the frequency increased from 0.1 to 100 Rad s^{-1}, the viscosity of both GelMA and GelMA-PPy hydrogels significantly decreased, representing shear-thinning and shear-thickening behavior. The viscosity of the GelMA and GelMA-PPy hydrogels at a high-frequency rate was 3.24 kPa and 5.17 kPa, respectively. Thus, the interaction of GelMA and PPy with Fe^{3+} ions results in a gel-fluid transition in the recorded range and displays suitable shear-thinning properties, crucial for 3D printing applications [49]. Previously, an ideal printing gel was considered to have both "*plug-like*" and "*Non-Newtonian* flow" [50–52]. To determine the flow behavior of the fabricated hydrogel inks, we examined the time-dependent fluidic nature of the hydrogel inks through a viscosity vs. shear rate plot (Fig. S4). The viscous flow behavior of our hydrogel inks was best fitted by both the Power-law equation [49] and Herschel–Bulkley fluid model [53]. For a typical shear-thinning gel, the flow consistency index k is denoted by the apparent viscosity of the hydrogel at a shear rate of 1 s^{-1}. Notably, the shear-thinning index n mainly governs whether the hydrogel is thinning ($n < 1$), thickening ($n > 1$), or Newtonian ($n = 1$) in nature. PPy incorporation into GelMA and Fe^{3+} addition increased n from 0.39 to 0.42 owing to the higher cross-linking and strong ionic interactions; however, both the GelMA and GelMA-PPy-Fe hydrogels displayed pseudoplastic flow behavior (Fig. S4a), favorable for 3D printing applications [54,55]. These results theoretically revealed the shear-thinning nature of the developed hydrogels under shear stress during extrusion. Furthermore, we investigated the yield stress of the developed hydrogels, and the results are shown in Fig. S4(b). We

observed an increased stress yield after adding PPy and post-cross-linking to GelMA-PPy-Fe hydrogels (~150,000 Pa s) compared to that in the pure GelMA (~120 Pa s). This was due to the rupture of the polymer network during extrusion and rejoining after deposition onto the platform. The incorporation of PPy into the GelMA matrix significantly improves the fluidity of the printable ink owing to the self-healing nature of the adjacent PPy chains [33]. Notably, the apparent viscosities of the hydrogels become similar at higher shear stresses, suggesting the complete rupture of the hydrogel network and rejoining after extrusion. A summary of the mathematical parameters used for the Power-law and Herschel–Bulkley models are presented in Table S4, respectively.

Next, we performed amplitude sweep studies for the fabricated hydrogels by subjecting the hydrogels to variable strains ranging from 0.1 to 100% and the results are showun in Fig. 2g. Both the fabricated hydrogels showed crossover point aound strain value of 100%. Within 100% strain, both the hydrogels showed comparable elesticity, making the hydrogels capable to withstand the strain caused during printing process.

The hydrogel inks' thixotropic behavior was measured in terms of the viscosity-time plot with rapid increase (0.1–1000 s^{-1}) and sudden decrease of shear rate (1000–0.1 s^{-1}). As shown in Fig. 2h, the η^* of GelMA-PPy-Fe hydrogel at 0.1 s^{-1} was 1.39 kPa, which was abruptly decreased to 2.67 Pa at 1000 s^{-1}, indicating the fluid-like nature. In contrast, as the shear rate jumped to 0.1 s^{-1}, η^* rapidly recovered to approximately 1.32 kPa. However, the GelMA hydrogel had an initial η^* of 0.29×10^3 Pa at 0.1 s^{-1}, 0.61 Pa at 1000 s^{-1}, and again 0.015×10^3 Pa, indicating the poor recovery rate compared to that of the GelMA-PPy-Fe hydrogels. Thus, our results suggest that the formulated GelMA-PPy-Fe ink has excellent shear-thinning and shear-recovery properties, which could benefit 3D printing applications.

Next, the mechanical properties of the developed hydrogel inks were evaluated using uniaxial tensile and compressive stress-strain measurements. Our results indicate that the GelMA-PPy-Fe has a maximum tensile strength (Fig. 2i) of 0.028 MPa (= 28 kPa) with Young's modulus of 0.16 kPa, much higher ($^*p < 0.05$) than the tensile strength of GelMA (= 0.15 kPa); this indicates that the GelMA hydrogel was semi-hard and fragile. The higher tensile modulus was due to the ionic cross-linking of gelatin and PPy with Fe^{3+} ions and their superior self-healing nature, making it more semi-IPN in nature than GelMA [33]. Uniaxial compressive tests (Fig. 2j) were performed to evaluate the compressive modulus and toughness of the prepared hydrogels. The compressive strength and toughness of the GelMA-PPy-Fe hydrogels were ~3.8 MPa and ~324 kJ m^{-3}, respectively, significantly higher than those of pure GelMA (~1.05 MPa and ~232 kJ m^{-3}). The compressive strength of the cross-linked GelMA-PPy-Fe hydrogel resembles that of human cancellous/trabecular bone (~0.1–16 MPa) [56], making it an ideal implantable material for bone tissue engineering applications [57,58]. The swelling behavior of the fabricated hydrogel scaffolds was evaluated at 37 °C for 50 h; the results are demonstrated in Fig. 2k. Owing to tight cross-linking and reduced porosity, GelMA-PPy-Fe exhibited less swelling than GelMA hydrogels. This was also reflected in the degradation behavior of the hydrogel scaffolds. The GelMA-PPy-Fe scaffolds displayed comparatively less degradation than the pure GelMA scaffold for up to 15 days of incubation in phosphate-buffered saline (PBS), suggesting higher mechanical stability (Fig. 2l). Magnetic nanocomposite materials have drawn enormous attention from researchers in bone regeneration therapy owing to their excellent biocompatibility and biosafety. Therefore, the controlled release of magnetic nanomaterials from scaffolds favors cellular growth and osteogenesis without adverse effects *in vivo* [59,60]. We investigated the release of Fe^{3+} ions as a function of time during the biodegradation study; the results are displayed in Fig. S5. Our results suggest that the Fe^{3+} ion release pattern was controlled for up to 15 days of incubation in PBS. Therefore, the superior mechanical properties, controlled biodegradation, and mineral release of the GelMA-PPy-Fe scaffold suggest its excellent use in bone tissue engineering applications.

The unique shear-thinning, shear recovery, and tunable mechanical properties motivated us to evaluate the printing properties of the developed hydrogel. First, we examined the injectability of the GelMA-PPy-Fe bioink to test its extrudability. As shown in Fig. S6(a–c), the hydrogel was sufficiently extruded from the needles and could flow appropriately without agglomeration or clogging at the end of the needle tip. As a proof of concept, we have shown that the "letter" (Fig. S6d) and "butterfly" (Fig. S6e) codes were successfully produced on a glass surface. Notably, the 20G (*d*: 0.60 mm), 21G (*d*: 0.50 mm), and 22G (*d*: 0.40 mm) needles have suitable extrudability; however, the 23G (*d*: 0.33 mm) needle was not suitable for injectability. We selected the 22G needle because of its ability to extrude uniform filaments during 3D printing. Fig. 3a presents an overview of the 3D printing procedure of the GelMA-PPy-Fe hydrogels using a 400-μm extrusion nozzle (22G) and the cross-linking procedure. As the GelMA-PPy-Fe hydrogel was extruded from the nozzle (extrusion pressure = 55 kPa), the ink underwent a steady-state liquid-like flow and immediately self-healed to form a stable filament after coming out from the nozzle. The filament length increased linearly ($R^2 = 0.99907$) by 30 mm. The extruded filament was immediately deposited onto a cooled print bed to solidify the filament (Fig. 3b). It is important to note that GelMA-PPy-Fe behaves like a complementary network ink, where GelMA contributes to the thermo-responsive gelation, and PPy contributes to the semi-IPN network upon ionic corsslinking [61,62]. Similarly, the height of the printed construct increased linearly ($R^2 = 0.9974$) as the construct height increased from 0 to 10 mm (Fig. 3c). The formation of stable filaments during 3D printing is directly related to the concentration of the fabricated ink and the surrounding temperature of the platform. Fig. 3d illustrates the extrudability of the GelMA-PPy hydrogel ink under varying temeprature range. The results demonstrated that the filament formation of GelMA-PPy is mainly dependent on the concentration and corresponding temperature [20,63,64]. At a low concentration (5–8 wt. %) and temperature (4 °C), the extruded filament is irregular due to the inherent physical cross-linking and fast flow nature. However, the extruded filament exhibited a suitable printing quality when the concentration rose from 10 to 15 to wt.% even at room temperature (25 °C). Likewise, at 5–8 wt.%, the GelMA-PPy ink is nearly inextrudable owing to its fluid-like nature. The digital images of the filament formation of various GelMA-PPy inks are skown in Fig. 3e. Notably, the fimanet dimeter of the GelMA-PPy greatly influenced by the printing temeprature. At low concentration (5–10%) and low temperature (4 °C) with an extrusion pressure 55 kPa, the fimanet dimater varied differently (irregular filaments) owing to the fast geletion and low shear stress (Fig. 3f). However, the flow consistency and stable filament formation was observed using 12 wt% and 15 wt% GelMA-PPy ink, suggesting that enhancing concentration not only promoted controlled gelation but also improved the self-healing property. Similarly, when the temeprature was increased from 4 °C to 15 °C–25 °C, low concentration inks produced filaments with greater diameter while the higher concentration inks exhibited stable filament formation (Fig. 3g). Therefore, 12–15% concentration of GelMA-PPy have excellent printability, and thus 15 wt % concentration was chosen for the 3D printing applications in our study. Digital photographs of the filament formation in 15 wt% GelMA-PPy ink as a function of time is shown in Fig. 3h. Furthermore, the stability of the extruded filament in body fluids is also crucial for 3D bioprinting and *in vivo* applications [64]. As shown in Fig. 3i and **Video S1**, the GelMA-PPy ink was more stable when directly extruded into PBS (pH 7.4) than GelMA. Thus, we conclude that the GelMA-PPy ink was highly stable and less degradable during 3D printing. A digital photograph of the 3D printing process in a 6-well cell culture plate is shown in Fig. 3j. To emphasize the structural stability, fresh printed (circular model, *l*: 1.5 cm, and *d*: 1 cm) GelMA-PPy-Fe hydrogels were fridge-dried, swelled for seven days, and subjected to uniaxial compressive loading tests. As shown in Fig. S7, the printed structures have superior mechanical stability even after soaking in PBS for seven

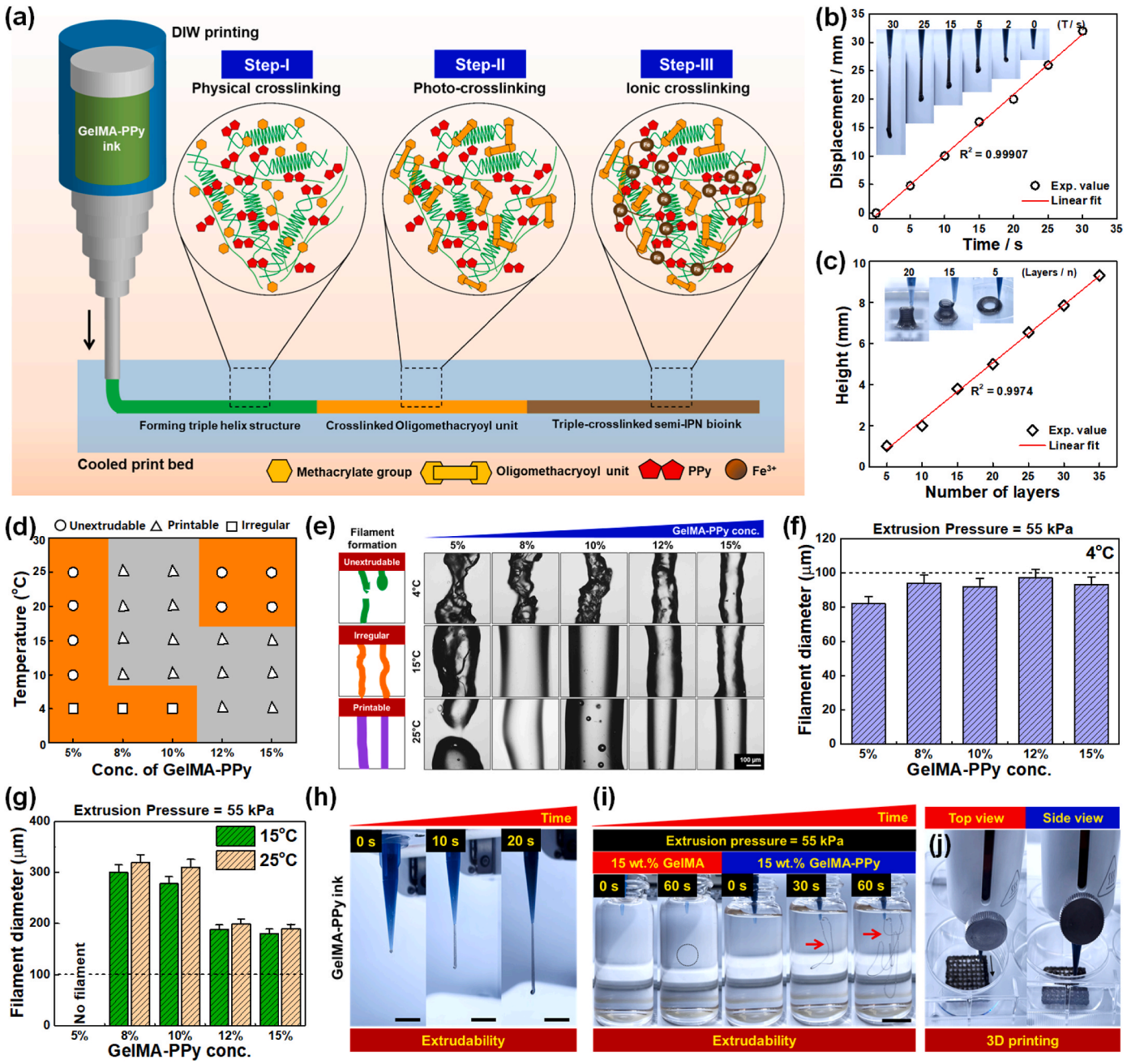

Fig. 3. Evaluation of printability of the GelMA-PPy hydrogel. **(a)** Schematic illustration of the ink deposition process. **(b)** The steady-state flow curve with a function of time for the GelMA-PPy hydrogel ink. **(c)** Correlation between layer height *vs.* number of layers as a function of printability. **(d)** The phase diagram showing the printability based on concertation *vs.* temperature profile of the GelMA-PPy ink. **(e–g)** Qualitative and quantitative evaluation of the filament formation under varying temperature. Scale bar: 100 μm. **(h)** Digital photographs of the extruded hydrogel at indicated time point showing the shear-thinning behavior. Scale bar: 0.5 mm. **(i)** The extrudability property of the GelMA and GelMA-PPy hydrogel ink in the PBS as a function of time, showing the stability of the filament. Barrel temperature was maintained at 4 °C. Scale bar: 10 mm. **(j)** Pictorial representation of the 3D printing process using GelMA-PPy hydrogel ink. Black arrowhead indicates the printing direction.

days, demonstrating their structural integrity. The wettablilty properties of the 3D printed GelMA and GelMA-PPy-Fe scaffolds were evaluated through contact angle measurement at room temeprature. As shwon in Fig. S8, the contact angle and surface energy of the pure GelMA scaffold was detected about 62° and 35.1 mN m^{-1} which was decreased to 48° and 48.71 mN m^{-1} in case of GelMA-PPy-Fe scaffolds. This result furthur indicate that the PPy incorporation and Fe^{3+} crosslinking changed the hydrophilicity of GelMA [65]. However, such change is negligible compared to the pure GelMA and our results are consistent with the swelling study.

Supplementary data related to this article can be found at https://doi.org/10.1016/j.biomaterials.2023.121999.

2.3. 3D printing of complex biological structures

The excellent stability, shear-thinning, fast self-healing, and stress-yielding properties of the developed GelMA-PPy-Fe hydrogel motivated us to evaluate the 3D printing of complex biological structures. As a proof of concept, we printed several biomimetic structures, such as square (10 layers), hexagonal infilled patterned structures (20 layers),

hollow cylinders (25 layers), and honeycomb lattice patterned structures (50 layers). The pure GelMA ink (15 wt%) was also printed side-by-side to compare the printability. Fig. 4a and **Video S2** show that all the printed structures were highly accurate and had outstanding printing quality without collapsed structure at 15 wt% GelMA-PPy concentration. Similarly, pure GelMA with 15 wt% concentration was printable but failed to demonstrate the high-resolution structures (Fig. S9a). We observed that approximately 5, 12, and 11 layers were printable for square, hexagonal, and cylindrical designs using GelMA ink. An overview of the 3D printing process of GelMA is presented in

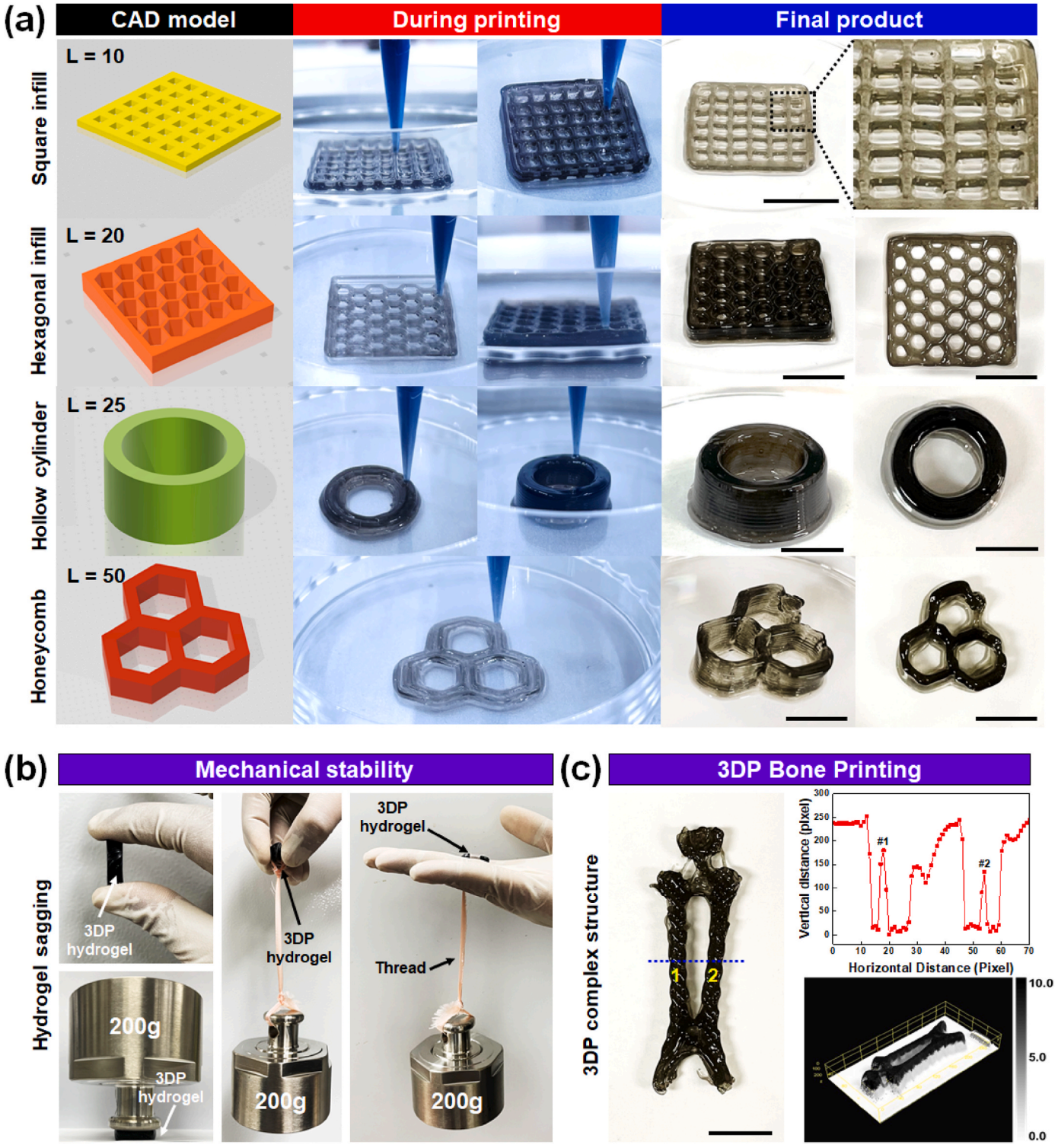

Fig. 4. 3D printing of complex architectures showing the mechanical integrity using GelMA-PPy bioink. Demonstration of square structure, hexagonal infill, hollow cylinder, and honeycomb structure. L represents the number of layers during 3D printing. Scale bar: 10 mm. **(b)** Weight lifting study to evaluate the mechanical stability of the 3D printed hydrogel. The 3D printing was performed using 90% infill density to maximize the mechanical performance. **(c)** Demonstration of a full-length rat bone structure using GelMA-PPy ink. The line-scan profile and 3D surface plot was measured to evaluate the printing quality of the construct. Data was analyzed using NIH ImageJ software (v1.8, NIH, Bethesda, USA).

Fig. S9(b). The printability of a given bioink is significantly affected by the designed structure [49], nozzle diameter [3,64], printing speed [49,64], and critical nozzle height (h_c) [35]. The latter mainly affects printability. We have calculated the h_c value for 400 μm printing nozzle to be approximately 6.5 ± 0.23 mm (fitting model: $y = -2.7872 + (1.09^*x + 0.931x^2)$, $R^2 = 0.9426$). We performed 3D printing using varying print speeds (2–12 mm s^{-1}) to support the mathematical calculations (Fig. S9c and Video S3). When $h_c \leq 6.5$ mm, the GelMA-PPy-Fe ink may give high-resolution 3D structures; however, a $h_c > 6.5$ mm will produce collapsed structure after carving 5–10 layers.

Supplementary data related to this article can be found at https://doi.org/10.1016/j.biomaterials.2023.121999.

To support the abovementioned findings, we printed more complex structures, such as a full-thickness rat bone model using the developed hydrogel ink. The developed hydrogel ink had a higher yield strength and superior recovery strength, enabling high-resolution complex 3D printing without a supporting bath [66,67]. Before demonstrating complex biological structure, we tested the mechanical stability of the 3D printed constructs using weight lifting method. As shown in Fig. 4b, the 3D printed and crosslinked hydrogel can withstand a load of 200 g, indicating the durablity of the fabricated sample.The rat bone model was first designed using SolidWorks software and then sliced using Slicr3D software. Next, the structure was printed onto a precooled platform, and the layer-by-layer structure took approximately 16 min to print. After 3D printing, the construct was ionically cross-linked and subjected to printability analysis. Fig. 4c shows that the GelMA-PPy-Fe hydrogel ink successfully printed the bone construct based on the designed structure. Moreover, the line-scan profile and 3D surface plot exhibited nearly perfect strands during the printing. Next, we tested the mecahnical and conductive property of the 3D printed hydrogels (square design as demonstrated in Fig. 4a). Three independent printed samples were selected to test the mechanical and conductive properties of the as-fabricated 3D hydrogels. As shown in Fig. S9d, the GelMA-PPy-Fe constructs displayed suitable stability, even after 14 days of incubation in PBS at 37 °C. The 3D printed strands were visible to the naked eye for GelMA-PPy-Fe gels; however, the pure GelMA hydrogels exhibited slight degradation followed by no observable 3D strands. These morphological examinations indicated that PPy addition and ionic cross-linking significantly improved the stability of the scaffolds in the aqueous medium. The PPy-containing hydrogels were also mechanically robust (Fig. S10a&b) and electrically conductive even after uniaxial compressive loading and unloading tests (Fig. S10c). Therefore, we anticipate that our formulated GelMA-PPy bioink will have excellent print fidelity and can be used to engineer several biomimetic structures for tissue engineering applications, especially for bone tissue engineering.

2.4. Device setup and optimization of electric field for cell culture

A direct-current stimulation device (EF device) was constructed to favor a small cell culture volume with a precise control system (Fig. S11a). The device was made with a stainless-steel lid and base (dimensions 147 mm × 105 mm × 60 mm) and designed for a 6-well plate cell culture (Fig. S11b). Each chamber consisted of two rectangular platinum plates, and each pair of plates was further connected to a standard electric power supply. The power supply was made using a digital wavefront generator (1-channel, 25 MHz, 250MSa s^{-1} sampling rate, Tektronix Inc., Oregon, USA) connected to a digital oscilloscope. Before cell culture, the inner and outer lids and platinum plates were sterilized using 70% alcohol, followed by a 24-h UV sterilization. Each cell cultured on the 3D printed hydrogel receives 250 mV/mm DC EFs stimulation for 20 min per day. All cell culture experiments were conducted at the desired time points, and EFs stimulation was constantly maintained throughout the experimental period.

2.5. In vitro bioactivity, 3D bioprinting, and osteogenic differentiation of stem cells

The *in vitro* culture procedure for hBMSCs in the presence of 3D printed scaffolds is schematically illustrated in Fig. 5a. We investigated the effect of EFs stimulation on both 2D (surface cell seeding) and 3D (cell-laden or cell-encapsulated 3D printing or 3D bioprinting) cell culture systems and their effect on the osteogenic differentiation of hBMSCs.

Before 2D/3D cell culture, we checked the cytotoxicity of hBMSCs in the presence of various EFs stimulations, such as 100 mV, 250 mV, and 500 mV/20 min/day. As shown in Fig. 5b, the viability of hBMSCs increased significantly in the presence of 250 mV/20 min/day stimulation, even after three days of culture. Therefore, 250 mV DC EFs stimulation is non-toxic to hBMSCs [8,9,68]. Similarly, both the GelMA and GelMA-PPy-Fe hydrogels were biocompatible and non-toxic to hBMSCs as indicated in Fig. 5c. Next, we performed a live–dead staining assay to confirm cell viability. Interestingly, the number of hBMSCs significantly increased in the presence of GelMA-PPy-Fe scaffolds with 250 mV EF stimulation (Fig. 5d). Therefore, we anticipate that our hydrogel scaffolds and the proposed EFs stimulation system will be physiologically safe for hBMSCs culture. Fig. 5e, f shows the FL images with corresponding quantification of the live-dead staining of hBMSCs seeded onto the GelMA and GelMA-PPy-Fe hydrogels. Interestingly, the number of cells was significantly higher by ~15% in the presence of GelMA-PPy-Fe even after EFs stimulation, suggesting the biocompatible nature of the conductive hydrogels [69]. The excellent biocompatibility of the fabricated hydrogel is also due to its superior adhesion, smart mechanotransduction, and fast metabolism of hBMSCs [70,71]. To investigate cell morphology, hBMSCs were stained with Actin Red, and images were captured using an inverted fluorescence microscope, and the results are shown in Fig. 5g. Notably, the actin alignment was guided by EFs stimulation. We observed differences in the cell shape cultured on the two hydrogels under EFs stimulation. Notably, cells were highly aligned in the GelMA-PPy-Fe hydrogels w.r.t. the GelMA counterpart under stimulated condition. We quantified this cellular morphometric changes in terms of their actin anisotropy. As shown in Fig. 5 (h, i), the randomness in the F-actin orientation was ~0.22% in the GelMA hydrogel which was ~0.13% in the GelMA-PPy-Fe hydrogel. Similarly, the percentage of aligned fibers was measured to be ~0.15% in the cells grown on GelMA hydrogels. However, the F-actin alignment was enhanced to ~0.70% in the GelMA-PPy-Fe hydrogel. Similar behavior was observed in the nuclear aspect ratio in the cells. The nuclei were highly elongated when cultured on GelMA-PPy-Fe hydrogels with the desired EFs stimulation even up to fifth day of cell culture. Therefore, 250 mV/20 min EF stimulation enhanced hBMSCs proliferation and guided cell migration in the presence of DC EFs.

Thus, we conclude that 250 mV/20 min/day stimulation on a 3DP scaffold is biologically safe and can be used as a microcurrent stimulation platform for stem cells undergoing osteogenesis [72,73].

The excellent biocompatibity of the GelMA-PPy-Fe hydrogel furthur motivated us to scrutinize their bioprintability. As shwon in Fig. 5j, the bioprinted hBMSCs were found healthy after 3 days of incubation. About ~93% of the cells were found viable after 3 days of bioprinting under EFs stimulation (Fig. 5k). It was interesting to note that hBMSCs strated proliferating and alinged to the bioprinted strand under exposure of EFs stimulation (Fig. 5l). The slow proliferation of the cells was probably due to the moderate high elastic moduli of the hydrogels. Nevertheless, we found higher viability of the bioprinted hBMSCs which is quaite good for bioprinting application.

Next, we evaluated the *in vitro* osteogenic differentiation of hBMSCs in the presence of GelMA and GelMA-PPy-Fe hydrogels using alizarin Red-S (ARS) staining. Before the EF-induced hydrogel-based cell culture, we examined the effect of the scaffolds on the osteogenic differentiation of hBMSCs. As shown in Fig. S12, the GelMA-PPy-Fe scaffolds exhibited better mineral induction efficiency than GelMA after 7 and 14 days of

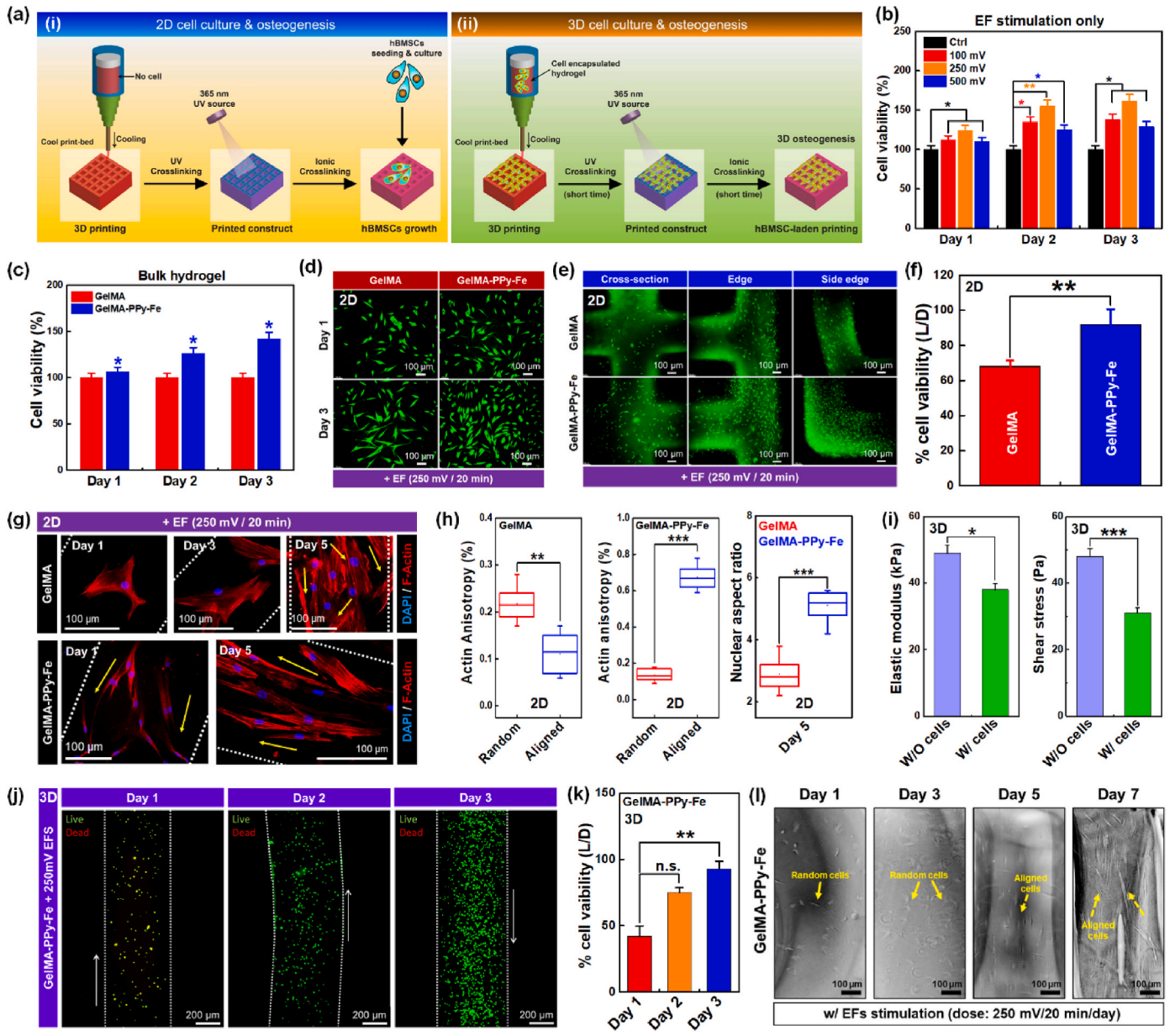

Fig. 5. *In vitro* biocompatibility and morphometric study of hBMSCs cultured on 3D printed hydrogels. **(a)** Schematic illustration of the cell culture procedure showing the protocol for **(i)** surface cell seeding (2D), and **(ii)** cell-laden culture (3D), respectively. **(b)** WST-8 viability assay of hBMSCs in the presence of EFs stimulation at indicated time intervals. **(c)** WST-8 assay of hBMSCs in the presence of GelMA and GelMA-PPy-Fe hydrogel under influence of 250 mV/20 min EF stimulation. **(d, e)** Representative Live/Dead assay of hBMSCs after EFs treatment on bulk hydrogel and 3D printed hydrogel after 3 days of incubation. Scale bar: 100 μm. **(f)** Quantification data of the Live/Dead assay. Scale bar: 100 μm. **(g)** Immunofluorescence staining showing the orientation of F-actin (red) and nucleus (blue) with corresponding actin anisotropy quantification and nuclear aspect ratio **(h)**. yellow arrow indicates printing direction. Scale bar: 100 μm. **(i)** The elastic modulus and shear stress of the GelMA-PPy bioink before and after hBMSCs loading. **(j, k)** Representative Live/Dead staining images with corresponding quantification data of 3D bioprinted hBMSCs after 5 days of incubation. White arrow indicates printing direction. Scale bar: 100 μm. **(l)** Optical micrographs showing the 3D bioprinted hBMSCs. Scale bar: 100 μm. Data reported as mean ± s.d. of triplicate experiments, statistical significance at $*p < 0.05$, $**p < 0.01$, and $***p < 0.001$ (ANOVA and Student *t*-test). (For interpretation of the references to color in this figure legend, the reader is referred to the Web version of this article.)

culture in osteogenic differentiation media. The hydrogel-based culture was divided into two groups: (1) 2D cell culture and (2) 3D cell culture. As shown in Fig. S13(a), the 2D cell culture of hBMSCs in the presence of EFs enhanced mineral induction with GelMA-PPy-Fe scaffolds, which was significantly higher than that of GelMA. ARS quantification of the 2D cell culture is shown in Fig. S13(b). Notably, the 3D bioprinted scaffolds (3D culture) promoted even better osteogenesis than the 2D culture in the presence of both GelMA and GelMA-PPy-Fe scaffolds after 14 days of osteogenic induction. Fig. S13(c) indicates that the 3D culture had a more intense ARS stain than the GelMA itself. The quantification of ARS nodule formation is shown in Figure S13(d). Optical micrographs of the 3D printed scaffolds near the cross-section and transverse section are shown in Fig. S13(e). White arrows indicate the formation of mineralized nodules.

The expression of osteogenesis-related genes **(Table S3)** and proteins **(Table S5)** was evaluated to confirm the osteogenic potential of the developed 3D printed hydrogels. Fig. S14 shows the fold change of the expression of genes encoding Runt-related transcription factor 2 (*Runx2*), alkaline phosphatase (*ALP*), osteocalcin (*OCN*), osteopontin (*OPN*), and bone sialoprotein (*BSP*) after 7 and 14 days of osteogenic

differentiation in the presence of 3D printed GelMA-PPy-Fe hydrogel. The control set represents the expression profile of GelMA. Interestingly, the expression of both early (*Runx2* and *ALP*) (Figs. S14a and b) and late gene (*OCN*, *OPN*, and *BSP*) (Figs. S14c–e) markers was significantly upregulated in 3D culture compared to 2D culture after 7 and 14 days of osteogenic induction. Therefore, we conclude that the developed 3D printed PPy-based GelMA scaffolds have excellent electrical and biological activity, promote osteogenic differentiation of stem cells, and help develop electrical stimuli-based bone tissue engineering platforms for treating bone diseases and inflammation.

2.6. Macropahge-assisted enhanced osteogenic activity

To access the *in vitro* immunomodulatory property of the of the developed hydrogels, we first investigated the monocyte/macrophage polarization potenial in the presence of GelMA and GelMA-PPy-Fe hydrogels. The experimental protocol is schematically illustrated in Fig. 6a. The Raw 264.7 cells were cultured for 48 h in the presence of GelMA and GelMA-PPY-Fe scaffolds and the phenotypic plasticity was examined using flow cytometry. As shown in Fig. 6b, the Raw cells were found positive for CD163 marker in the presence both scaffolds, but the

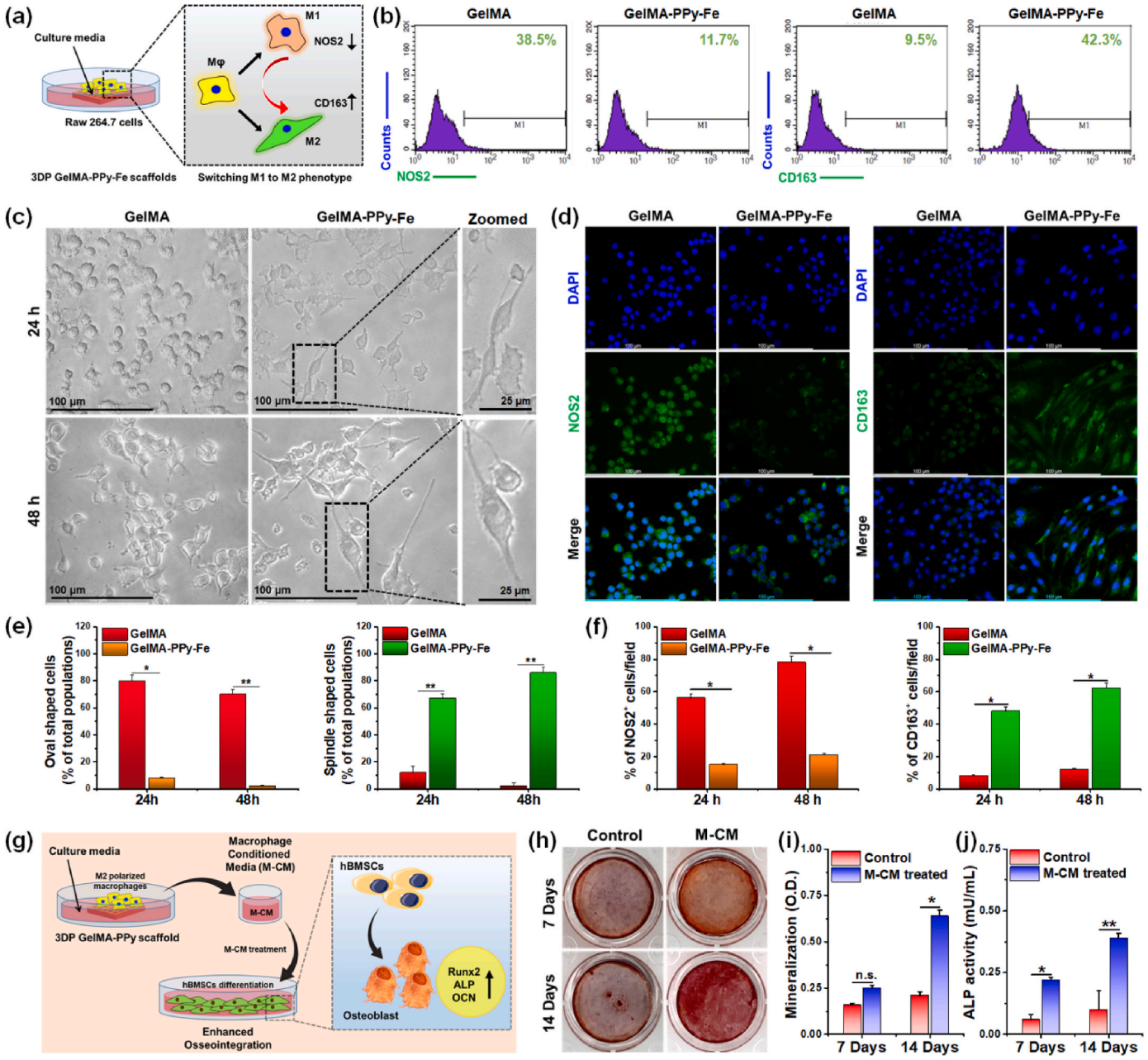

Fig. 6. Macrophage polarization and osseointegration potential of the fabricated scaffolds. **(a)** Schematic illustration of the experiment. **(b)** Flow cytometry analysis of the Raw 264.7 cells for NOS2 (M1 marker) and CD163 (M2 marker). **(c)** The morphology of the Raw 264.7 cells cultured with the fabricated hydrogels at indicated time points. **(d)** Representative FL microcopy images of Raw 264.7 cells showing the cellular expression of NOS2 and CD163 (green color) after 24 h of culture. **(e)** Quantitative evaluation of the percentage of oval and spindle-shaped Raw 264.7 cells during immunomodulation. **(f)** Quantification of the NOS2 and CD163 cells after 24 h of immunopolarization. **(g)** Schematic illustration for osteo-immunomodulation experiment. **(h)** ARS staining of hBMSCs in the presence of M-CM after 14 days of treatment. **(i, j)** Quantification of ARS and ALP activity of the hBMSCs in the presence of M-CM. Scale bar: 25 and 100 µm. Data reported as mean ± s.d. of triplicate experiments, statistical significance at $^{*}p < 0.05$ and $^{**}p < 0.01$ (Student *t*-test). (For interpretation of the references to color in this figure legend, the reader is referred to the Web version of this article.)

percentage of expression was higher in the presence of GelMA-PPy-Fe than pure GelMA. Similarly, the expression of iNOS(NOS2) was also found higher in the presence of pure GelMA, followed by a low expression profile in the presence of GelMA-PPy-Fe. These results suggest that the GelMA-PPy-Fe scaffold have the potential to modulate M2 polarization of Raw 264.7 cells. To confirm furthur, we investigated the morphological changes of Raw 264.7 cells during 48 h of culture. Notably, the Raw 264.7 cells exhibited oval to cyllindrical morphology in the presence of pure GelMA scaffold after 48 h of incubation. However, the Raw 264.7 cells growing onto the GelMA-PPy-Fe scaffold displayed an elongated or rod-shaped fibrobalstic morphology, suggesting the M2 polarized state after 48 h of incubation (Fig. 6c). The qunatification data of the morphological study is given in Fig. 6e. The immunocytochemical analysis also revealed similar results which are well accordnace with the cytometry data. As shown in Fig. 6d, the GelMA-treated cells exhibited a strong cytoplasmic fluorescence (FL) for NOS2 (green), whereas the GelMA-PPy-Fe-treated cells displayed a weak signal for NOS2. On the other hand, the Raw 264.7 cells were foundly highly positive for CD163 in the presence of GelMA-PPy-Fe, which was characterized by the strong FL signals from the cytoplasam. The quantitative data for the ICC staining is given in Fig. 6f.

Based on the above-mentioned results, we assumed that the GelMA-PPy-Fe hydrogel might promote the osteo-immunomodulation through M2 polarization of macrophages. The detailed experimental procedure of osteo-immunomodulation is schematically shown in Fig. 6g. The macrophage-derived conditioned media (M-CM) of GelMA-PPy-Fe was used for osteogenesis study. The plated withoutout M-CM were considered as control groups. Interestingly, the hBMSCs were able to differentiated into osteobalst and displayed higher mineral deposition after 14 days in the presence of M-CM than control media (Fig. 6h), suggesting that the M-CM had positive role in hBMSCs differentiation. The quantification data of the ARS staining in the presence or absence of M-CM is given in Fig. 6i. To investigate the ALP activity, we harvested the hBMSCs after 7 and 14 days of osteo-induction and measured the cellular ALP content. As shown in Fig. 6j, the M-CM treatment significantly (**$p < 0.01$) raised the ALP activity than control groups. Taken together, our results demonstrate that the developed hydrogel (GelMA-PPy-Fe) was non-toxic to the Raw 264.7 cells and induced the M2 polarization, which in trun boosted the osteogenic potential of hBMSCs.

2.7. 3D culture model exhibited distinct transcriptomic profiles

To evaluate the transcriptomic and proteomic changes, we developed three independent models: (1) TCPS control group (without scaffolds), (2) 2D culture group (hBMSCs seeded onto the printed hydrogels), and (3) 3D culture group (3D bioprinted). We cultured hBMSCs in osteogenic induction media for seven days and performed global transcriptomic profiling using RNA sequencing (RNA-seq) analysis (Fig. S15a). The Venn diagram obtained from RNA-seq revealed drastic transcriptomic changes in the control and treatment groups. A total of 203 and 1561 genes were significantly up- and contra-regulated, respectively, in EF-stimulated 3D culture; however, only 127 and 1472 genes were found in the control group (Fig. S15b). Interestingly, 271 and 461 genes were upregulated and downregulated in the 2D culture groups, respectively. Moreover, only 35 and 41 genes were upregulated in the 3D and 2D culture groups, respectively, compared to the control sets. Approximately 2317 and 476 genes were significantly downregulated in the 3D and 2D cell culture groups, respectively, compared to that in the control group (1797 genes). Next, we analyzed the differentially expressed genes (DEGs) to evaluate the specific pathway related to the genes upregulated or downregulated during EF stimulation in different culture conditions.

We also noticed a significant variation in major biological functions, such as RNA metabolism, extracellular matrix (ECM) secretion, mesenchymal cell differentiation, immune response, and secretion during 2D and 3D cell culture of hBMSCs compared to that in the control groups. Notably, the 3D culture system significantly enhanced (average clustering co-efficient 0.596; FDR *$p < 0.05$) the early expression of *EDC* (a positive regulator of p53/TP53), ZPR1 (zinc finger protein R1), *CDK12* (cyclin-dependent kinase 12), and *RBMX* (heterogeneous nuclear ribonucleoprotein) compared to the control groups. Previously, it was demonstrated that *CDK12* [74] and *RBMX* [75] are mainly activated by the presence of various biopolymer materials. Similarly, the expression of matrix-related genes, such as *COL* (collagen) and transforming growth factor (*TGF*), was also high during the 3D culture of hBMSCs. In addition, several DEGs related to ECM function (*COL3A1, COL4A1, COL5A1, COL7A1, COL8A2, COL11A1, COL14A1, COL15A1, TGFB1*, *TGFB2, CXCL14, CXCL12, VEGFA*) (Fig. S15c), cell differentiation (*EGFR, RUNX2, FOXO3, SOX4, SOX 12, NOTCH1* and *NOTCH2*), and immune response or secretion (*IL6, IL6R, CXCL3, CXCL6, CXCL8, CXCL12, CXCL14, CXCL16, IL4R, CCL7,* and *CCL8*) that were significantly upregulated during 3D cultures system were not found in 2D culture or control groups, suggesting that 3D encapsulation of hBMSCs into GelMA-PPy-Fe hydrogel potentially stimulated the ECM protein secretion, immunopolarization, and bone remodeling factors, consistent with previous reports [6,76,77]. Furthermore, a range of angiogenic genes were significantly (*$p < 0.05$) upregulated (*SEMA5A, MMP19, VEGFB, CXCL8, PDGFRA, AKT1, ANGPTL2*, and *TGFB*) and downregulated (*ADIPOR2, NUS1*, and *ANPEP*) during the 3D culture of hBMSCs under EFs stimulation (Fig. S15d). These results indicate that the encapsulated hBMSCs in the bioprinted GelMA-PPy-Fe hydrogel underwent mesenchymal-to-endothelial transition during osteogenesis [78]. Owing to the biocompatible nature of the hydrogel ink, we also noticed that a range of transcription factors that were actively related to "cell migration" were significantly (*$p < 0.05$) upregulated (Fig. S15e), suggesting that EFs stimulation affected the cell proliferation, migration, and osteogenic differentiation of hBMSCs [79–81]. A comparative result of the percentage of total significant genes upregulated in various biological processes is given in Figs. S15(f and g). Concurrently, we found that several epigenetic factors, such as lysine demethylase (*KDM6B*), histone deacetylase (*HDAC5*), and DNA methyltransferase (*DNMT3A* and *DNMT3B*) were either up or downregulated (Fig. S16) during 3D culture of hBMSCs compared to 2D or control groups, suggesting the enhancement of osteogenic properties [82,83].

Next, we investiaged the transcriptomic changes in osteobalst differentiation in various treatment groups. *K*-means hierarchical clustering (Fig. 7a) relvelaed the major role of EFs stimulation on osteobalst differentiation. Among the 4 different clusters, the cluster A and B showed the presence of osteoblast specific DEGs related to 'osteobalst differentiation', 'osteobalst proliferation', 'osteobalst development', 'cell surface receptor signaling', 'bone metabolism', and 'bone mineralization' terms. The cluster C and D represented the least expressed DEGs related to osteobalst differentiation. Interestingly, in cluster A and B, the expression of *CBFB, MAPK14, ERK-1/2, SMAD2, SMAD5, VEGF, RUNX2, OCN, COL1A2, ALP, BMP2, BMP6*, and *GDF2* were found significantly higher (Log2fold, *$p < 0.05$) in 3D culture group that control and 2D culture group (Fig. 7b), meaning that 3D culture of hBMSCs inside GelMA-PPy-Fe hydrogel promoted the expression of differentiation specific genes, while downregulated the proliferation gene markers. To verify the RNA-seq data, we furthur analyzed the expression profile of various proliferation/differentiation markers using ICC, qRT-PCR and western blotting. As shown in Fig. 7c, compared to the control (GelMA), the 3D culture group exhibited higher FL intensity in Ki67 (yellow), Runx2 (green), and OCN (red) expression under 250 mV EF stimulation. The qRT-PCR results also demonstrated the higher fold expression of *Ki67* (1.1 fold), *Runx2* (0.5 fold), and *OCN* (0.8 fold) gene markers after 7 days, which were in accordance with the ICC results. To evaluate the osteogenic markers expression in protein level, we furthur fermored western blotting, and the results are displayed in Fig. 7d. Interestingly, the EFs stimulation through conductive GelMA-PPy-Fe hydrogel induced the accumulation of Runx2 and OCN proteins than control group, suggesting that EFs stimualtion had a positive

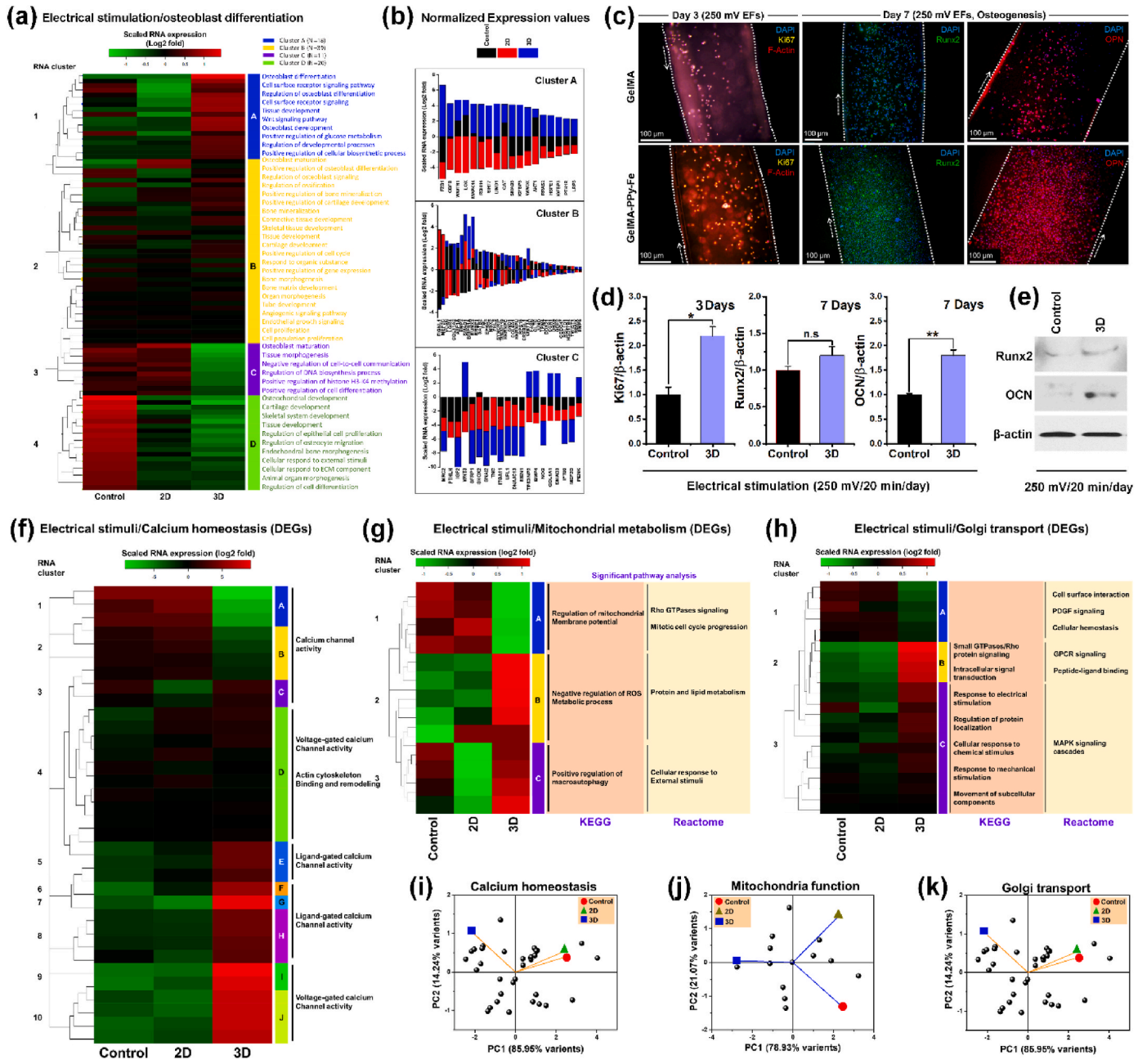

Fig. 7. Transcriptomic analysis of hBMSCs undergoing osteogenic differentiation in the presence of electrical stimulation. **(a)** *K*-means clustering heatmap of the DEGs associated with osteoblast differentiation under 250 mV EF stimulation up to 7 days. **(b)** Normalized RNA expression (Log2 fold, $^*p < 0.05$) of the DEGs from cluster 1, 3, and 4 showing the major changes during osteoblast differentiation. **(c–e)** Representative FL microscopy images of the hBMSCs showing the expression of proliferation marker (Ki67) and osteogenic markers (Runx2 and OCN) at indicated time points. The qRT-PCR results showing the expression of *Ki67*, *Runx2*, and *OCN* gene markers at indicated time points. Western blotting analysis of Runx2 and OCN after 7 days of EFs stimulation. **(f)** *K*-means clustering heatmap showing the major DEGs associated with calcium signaling/calcium homeostasis during EFs stimulation. **(g, h)** Clustering analysis of major metabolic (mitochondrial) and protein transport (Golgi transport) pathways of hBMSCs during EFs stimulation. **(j)** Principle component analysis (PCA) of the hBMSCs during metabolism under EFs stimulation. Scale bar: 100 μm. Data reported as mean ± s.d. of triplicate experiments, statistical significance at $^*p < 0.05$ and $^{**}p < 0.01$ (Student *t*-test).

role in osteogenic differentiation.

Previous studies showed that calcium homeostasis, mitochondrial metabolism, and endomemenrane transport had positive role in osteogenic differention under EFs stimulation [9,84]. To understand the effects of EFs on hBMSCs, we furthur screened transcritomic data. As shown in Fig. 7f, the *K*-means clustering revelated the presence of a bunch of DEGs associated with 'calcium channel activity', 'voltage-gated calcium channel activity', and 'calcium ligand binding activity' under EFs stimulation, similar to our previous report [9]. Similarly, EFs stimulation through 3D bioprinted hydrogel also enhannced the expression of various mitochondria and golgi transport-associated DEGs during osteogenic differention of hBMSCs (Fig. 7g and h). Kyota encyclopedia of genes and genomes (KEGG) and REACTOME pathway analysis also releaved that these genes were actually associated with mitochondrial memebrane potential (MMP) through Rho GTPase signaling, platelet derived growth factor (PDGF) signaling, G-protein coupled receptor (GPCR) signaling, and MAPK signaling, respectively. To identify the potential role of these metabolic pathways with osteogenesis, we furthur investigaed profrmed bioinformatic analysis. Principle component analysis (PCA) analysis showed that in 3D culture group, most of the

DEGs associated with calcium homeostasis were not clustered together, suggesting in involmenet of more than two siganling pathways (Fig. 7i). However, the PCA plot for control and 2D group exhibited in same cluster, meaning that they might share similar transcriptome during osteogenic signaling. A similar trend was observed in the PCA plot (Fig. 7j and k) of mitochondria and golgi-associated DEGs suggesting the involvement of more than two signaling pathways during osteogenesis.

2.8. 3D culture model sustains osteogenic capacity of hBMSCs via activating SMAD/NOTCH signaling pathways

To further evaluate the biological and molecular functions of the 3D culture model of hBMSCs, we performed gene set enrichment analysis (GSEA), gene ontology (GO), and qRT-PCR analysis. GSEA analysis revealed that the 3D bioprinted hBMSCs highly expressed gene hallmarks of NOTCH signaling (Figs. S17a and c) and downregulated the Wnt/β-catenin signaling pathway during osteogenic differentiation compared to the 2D culture model, suggesting that the 3D culture model sustains the native microenvironment of the bone matrix [85,86]. Similarly, several GO terms, such as DNA fragmentation, DNA methylation, DNA damage, apoptotic pathways, and muscle differentiation, were downregulated in the 3D culture model. We also observed an upregulation of MAPK/ERK and SMAD-1/2 signaling pathways (Figs. S17b and d) during electrical stimulation of hBMSCs in the 3D culture model, suggesting that these pathways actively participated during cell-material interaction and in response to extracellular biophysical stimuli, as reported previously [87,88]. We further demonstrated that PPI enrichment for the 2D culture system of hBMSCs revealed 139 DEGs associated with various biological processes, such as metabolic process, cell component organization, extracellular signal processing, ECM function, and protein binding activity. However, the 3D culture model of hBMSCs revealed an enhancement of PPI enrichment (total of 818 DEGs) for cell differentiation, metabolic process, cell proliferation, cell component organization, extracellular component, and molecular function.

To verify the signaling mechanism during osteogenesis, we also compared the RNA-seq data with qRT-PCR and human phosphorylation array data and the results are displayed in Fig. 8. We have selected the 5 genes from NOTCH pathway (*NOTCH1*, *NOTCH2*, *NOTCH3*, *NOTCH4, and Jagged1*), 1 gene from SMAD pathway (*SMAD1*), and 2 genes from MAPK pathway (*ERK1/2* and *p38 MAPK*) for qRT-PCR analysis owing to their greater expression on the transcriptomic data. As shown in Fig. 8a, the *NOTCH* related genes showed signficant difference on expression profile after 24 h of EFs stimulation within bioprinted hydrogel. Interestingly, a significant reduction in *NOTCH1* and *NOTCH3* was observed, while an enhancement of *NOTCH2* and *NOTCH4* was observed. On the

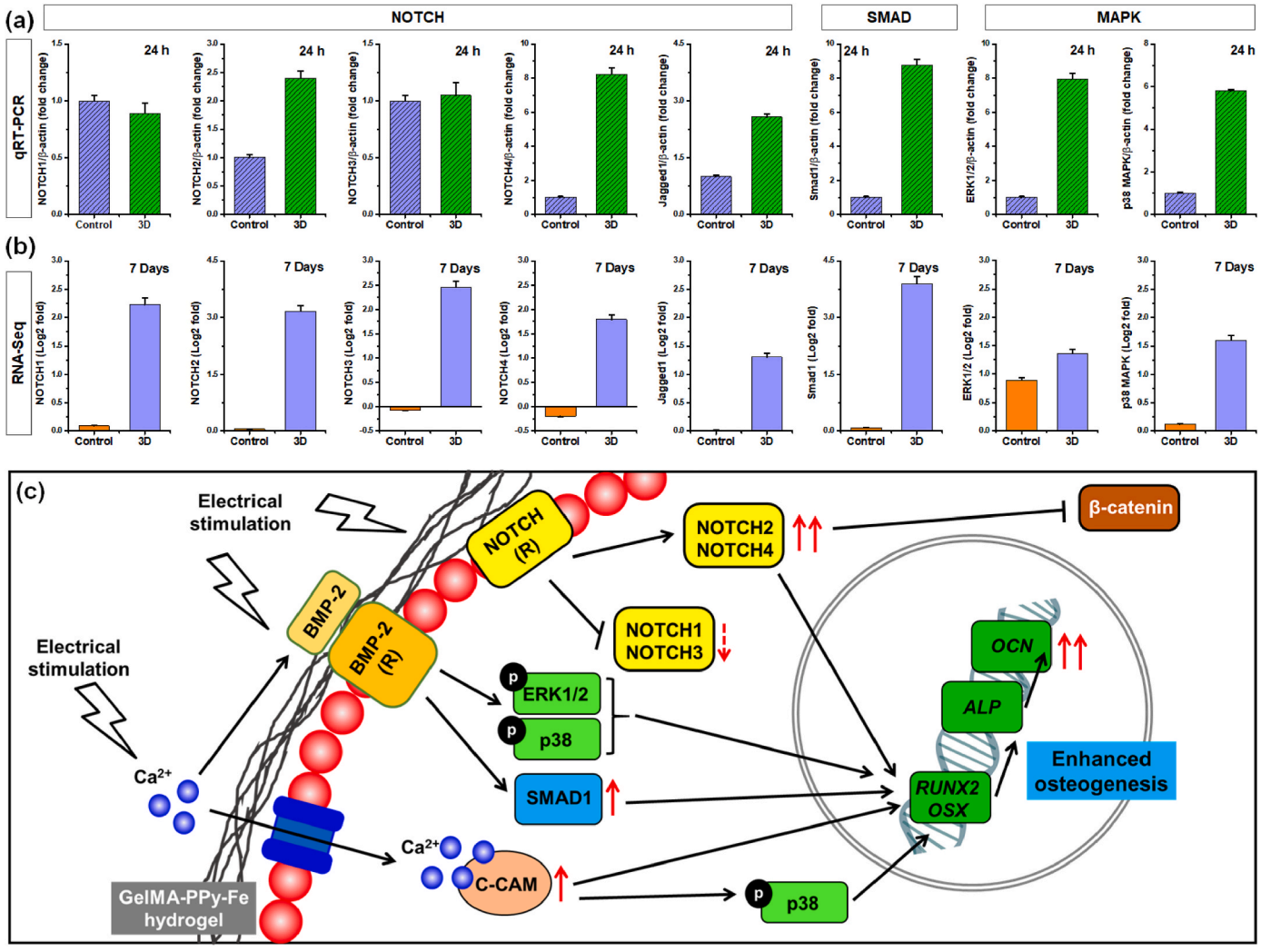

Fig. 8. Genomic and proteomic analysis of the hBMSCs in various culture condition under influence of EFs stimulation. **(a)** qRT-PCR analysis of hBMSCs related to NOTCH, MAPK, and SMAD signaling pathway w/EFs stimulation. **(b)** Normalized expression of NOTCH, MAPK, and SMAD signaling-related genes predicted through RNA-Seq analysis. **(c)** A hypothetical diagram showing the mechanism of osteogenic signaling through GelMA-PPy-Fe hydrogel in hBMSCs.q analysis. **(c)** A hypothetical diagram showing the mechanism of osteogenic signaling through GelMA-PPy-Fe hydrogel in hBMSCs.

other hand, no significant difference in *Jagged1* expression was observed compared to control group. Similarly, the expression of *SMAD1* was also upregulated in the 3D culture group compared to the control group which was well accordance with RNA-seq data (Fig. 8b). It is well known that electrical stimulation enhanced the early activation of BMP-2 receptor (BMP-2R) which promotes SMAD phosphorylation and activation of *Runx2* transcription factor [89]. Concurrently, we also observed an enhancement of MAPK gene markers, such as *ERK1/2* and *p38 MAPK*, during SMAD activation, demonstrating the direct role of SMAD and MAPK signaling through GelMA-PPy-Fe hydrogel. A hypothetical diagram shwoing the effects of EFs stimulation through conductive hydrogel and osteogenic signaling is shown in Fig. 8c. These results indicate that the 3D bioprinted GelMA-PPy-Fe hydrogel could recapitulate the native bone microenvironment, and EFs stimulation significantly enhanced the osteogenic potential of hBMSCs, which could be benificial for developing next-generative stimuli-assisted platforms for bone regeneration.

3. Conclusion

The present study demonstrates the fabrication of a highly conductive and shear-responsive GelMA-PPy-Fe bioink using a triple crosslinking (thermo-photo-ionic) strategy for DIW-based 3D printing applications. The as-fabricated hydrogel ink is programmable, injectable, shear-thinning, and stress-yielding, allowing higher print fidelity via "*plug-like Non-Newtonian*" flow. The power-law model and Herschel–Bulkley mathematical modeling for the GelMA-PPy-Fe bioink demonstrated the improved rheological and mechanical performance required for an ideal bioink. The 3D bioprinting of hBMSCs (3D culture model) allowed manipulation of the native extracellular microenvironment. It exhibited distinct transcriptomic signatures of the natural bone matrix via upregulating the *NOTCH/MAPK/SMAD* signaling, downregulating the *Wnt/β*-catenin signaling pathways and epigenetic modulators. External microcurrent stimulation in the 3D culture model also improved cytocompatibility, cellular migration, mesenchymal-to-epithelial transition, and enhanced osteogenesis of hBMSCs. The ability to manipulate the hBMSCs microenvironment *via* the conductive GelMA-PPy-Fe bioink will create a new approach towards stem cell-based therapy, especially for bone tissue-related therapeutics.

Credit author statement

Sayan Deb Dutta: Conceptualization, Methodology, Visualization, Writing – original draft, Formal analysis.Keya Ganguly: Visualization, Methodology, Formal analysis, Writing – review & editing.Aayushi Randhawa: Methodology, Formal analysis. Tejal V. Patil: Writing – review & editing. Dinesh K Patel: Formal analysis, Visualization, Writing – review & editing. Ki-Taek Lim: Supervision, Project administration, Funding acquisition.

Declaration of competing interest

The authors declare that they have no known competing financial interests or personal relationships that could have appeared to influence the work reported in this paper.

Data availability

Data will be made available on request.

Acknowledgments

This work was supported by the Starting Growth Technological R&D program (S2840309, Development of a novel bioreactor system with stimuli for stem cell cultures) funded by the Small and Medium Business Administration (SMBA), and was also funded by the Basic Science Research Program' through the 'National Research Foundation of Korea' funded by the Ministry of Education (NRF-2018R1A16A1A03025582, NRF- 2019R1D1A3A03103828, and NRF- 2022R1I1A3063302)

Appendix ASupplementary data

Supplementary data to this article can be found online at https://doi.org/10.1016/j.biomaterials.2023.121999.

References

[1] Y. Chen, J. Zhang, X. Liu, S. Wang, J. Tao, Y. Huang, et al., Noninvasive in vivo 3D bioprinting, Sci. Adv. 6 (2020), eaba7406.
[2] C. Wang, W. Huang, Y. Zhou, L. He, Z. He, Z. Chen, et al., 3D printing of bone tissue engineering scaffolds, Bioact. Mater. 5 (2020) 82–91.
[3] S.D. Dutta, J. Hexiu, D.K. Patel, K. Ganguly, K.-T. Lim, 3D-printed bioactive and biodegradable hydrogel scaffolds of alginate/gelatin/cellulose nanocrystals for tissue engineering, Int. J. Biol. Macromol. 167 (2021) 644–658.
[4] M. Qu, C. Wang, X. Zhou, A. Libanori, X. Jiang, W. Xu, et al., Multi-dimensional printing for bone tissue engineering, Advanced Healthcare Materials 10 (2021), 2001986.
[5] G.L. Koons, M. Diba, A.G. Mikos, Materials design for bone-tissue engineering, Nat. Rev. Mater. 5 (2020) 584–603.
[6] C. He, L. Yu, H. Yao, Y. Chen, Y. Hao, Combinatorial photothermal 3D-printing scaffold and checkpoint blockade inhibits growth/metastasis of breast cancer to bone and accelerates osteogenesis, Adv. Funct. Mater. 31 (2021), 2006214.
[7] S. Bose, S. Vahabzadeh, A. Bandyopadhyay, Bone tissue engineering using 3D printing, Mater. Today 16 (2013) 496–504.
[8] S.D. Dutta, J. Bin, K. Ganguly, D.K. Patel, K.-T. Lim, Electromagnetic field-assisted cell-laden 3D printed poloxamer-407 hydrogel for enhanced osteogenesis, RSC Adv. 11 (2021) 20342–20354.
[9] S.D. Dutta, T. Park, K. Ganguly, D.K. Patel, J. Bin, M.-C. Kim, et al., Evaluation of the sensing potential of stem cell-secreted proteins via a microchip device under electromagnetic field stimulation, ACS Appl. Bio Mater. 4 (2021) 6853–6864.
[10] X. Liu, M.N. George, S. Park, A.L. Miller II, B. Gaihre, L. Li, et al., 3D-printed scaffolds with carbon nanotubes for bone tissue engineering: fast and homogeneous one-step functionalization, Acta Biomater. 111 (2020) 129–140.
[11] S. Wang, J. Xu, W. Wang, G.-J.N. Wang, R. Rastak, F. Molina-Lopez, et al., Skin electronics from scalable fabrication of an intrinsically stretchable transistor array, Nature 555 (2018) 83–88.
[12] Y. Liu, J. Liu, S. Chen, T. Lei, Y. Kim, S. Niu, et al., Soft and elastic hydrogel-based microelectronics for localized low-voltage neuromodulation, Nature biomedical engineering 3 (2019) 58–68.
[13] H. Sirringhaus, T. Kawase, R. Friend, T. Shimoda, M. Inbasekaran, W. Wu, et al., High-resolution inkjet printing of all-polymer transistor circuits, Science 290 (2000) 2123–2126.
[14] Y. Wang, C. Zhu, R. Pfattner, H. Yan, L. Jin, S. Chen, et al., A highly stretchable, transparent, and conductive polymer, Sci. Adv. 3 (2017), e1602076.
[15] H. Yuk, B. Lu, S. Lin, K. Qu, J. Xu, J. Luo, et al., 3D printing of conducting polymers, Nat. Commun. 11 (2020) 1–8.
[16] K. Hong, Y.H. Kim, S.H. Kim, W. Xie, W.D. Xu, C.H. Kim, et al., Aerosol jet printed, Sub-2 V complementary circuits constructed from P-and N-type electrolyte gated transistors, Adv. Mater. 26 (2014) 7032–7037.
[17] L.-M. Yu, J.-X. Man, T. Chen, D. Luo, J. Wang, H. Yang, et al., Colorful conducting polymers for vivid solar panels, Nano Energy 85 (2021), 105937.
[18] H. Wei, M. Lei, P. Zhang, J. Leng, Z. Zheng, Y. Yu, Orthogonal photochemistry-assisted printing of 3D tough and stretchable conductive hydrogels, Nat. Commun. 12 (2021) 1–10.
[19] S. Samimi Gharaie, A. Seyfoori, B. Khun Jush, X. Zhou, E. Pagan, B. Godau, et al., Silicate-based electro-conductive inks for printing soft electronics and tissue engineering, Gels 7 (2021) 240.
[20] T. Distler, A.A. Solisito, D. Schneidereit, O. Friedrich, R. Detsch, A.R. Boccaccini, 3D printed oxidized alginate-gelatin bioink provides guidance for C2C12 muscle precursor cell orientation and differentiation via shear stress during bioprinting, Biofabrication 12 (2020), 045005.
[21] J. Kwon, C. DelRe, P. Kang, A. Hall, D. Arnold, I. Jayapurna, et al., Conductive ink with circular life cycle for printed electronics, Adv. Mater. (2022), 2202177.
[22] G. Basara, M. Saeidi-Javash, X. Ren, G. Bahcecioglu, B.C. Wyatt, B. Anasori, et al., Electrically conductive 3D printed Ti3C2Tx MXene-PEG composite constructs for cardiac tissue engineering, Acta Biomater. 139 (2022) 179–189.
[23] T. Distler, C. Polley, F. Shi, D. Schneidereit, M.D. Ashton, O. Friedrich, et al., Electrically conductive and 3D-printable oxidized alginate-gelatin polypyrrole: PSS hydrogels for tissue engineering, Advanced Healthcare Materials 10 (2021), 2001876.
[24] E. Fantino, A. Chiappone, I. Roppolo, D. Manfredi, R. Bongiovanni, C.F. Pirri, et al., 3D printing of conductive complex structures with in situ generation of silver nanoparticles, Adv. Mater. 28 (2016) 3712–3717.
[25] L.V. Kayser, D.J. Lipomi, Stretchable conductive polymers and composites based on PEDOT and PEDOT: PSS, Adv. Mater. 31 (2019), 1806133.
[26] A.R. Spencer, E. Shirzaei Sani, J.R. Soucy, C.C. Corbet, A. Primbetova, R.A. Koppes, et al., Bioprinting of a cell-laden conductive hydrogel composite, ACS Appl. Mater. Interfaces 11 (2019) 30518–30533.

[27] H. Rastin, B. Zhang, A. Mazinani, K. Hassan, J. Bi, T.T. Tung, et al., 3D bioprinting of cell-laden electroconductive MXene nanocomposite bioinks, Nanoscale 12 (2020) 16069–16080.

[28] M. Bordoni, E. Karabulut, V. Kuzmenko, V. Fantini, O. Pansarasa, C. Cereda, et al., 3D printed conductive nanocellulose scaffolds for the differentiation of human neuroblastoma cells, Cells 9 (2020) 682.

[29] S. Mehrotra, R.D. Singh, A. Bandyopadhyay, G. Janani, S. Dey, B.B. Mandal, Engineering microsphere-loaded non-mulberry silk-based 3D bioprinted vascularized cardiac patches with oxygen-releasing and immunomodulatory potential, ACS Appl. Mater. Interfaces 13 (2021) 50744–50759.

[30] B. Geng, F. Fang, P. Li, S. Xu, D. Pan, Y. Zhang, et al., Surface charge-dependent osteogenic behaviors of edge-functionalized graphene quantum dots, Chem. Eng. J. 417 (2021), 128125.

[31] K. Yue, G. Trujillo-de Santiago, M.M. Alvarez, A. Tamayol, N. Annabi, A. Khademhosseini, Synthesis, properties, and biomedical applications of gelatin methacryloyl (GelMA) hydrogels, Biomaterials 73 (2015) 254–271.

[32] J. Liu, L. Li, H. Suo, M. Yan, J. Yin, J. Fu, 3D printing of biomimetic multi-layered GelMA/nHA scaffold for osteochondral defect repair, Mater. Des. 171 (2019), 107708.

[33] S. Wang, J. Lei, X. Yi, L. Yuan, L. Ge, D. Li, et al., Fabrication of polypyrrole-grafted gelatin-based hydrogel with conductive, self-healing, and injectable properties, ACS Applied Polymer Materials 2 (2020) 3016–3023.

[34] D.K. Patel, S.D. Dutta, J. Hexiu, K. Ganguly, K.-T. Lim, 3D-printable chitosan/silk fibroin/cellulose nanoparticle scaffolds for bone regeneration via M2 macrophage polarization, Carbohydr. Polym.281 (2022) 1–18.

[35] J. Wang, L.L. Shaw, Rheological and extrusion behavior of dental porcelain slurries for rapid prototyping applications, Mater. Sci. Eng., A 397 (2005) 314–321.

[36] H. Mohammadi, M. Sepantafar, N. Muhamad, A. Bakar Sulong, How does scaffold porosity conduct bone tissue regeneration? Adv. Eng. Mater. 23 (2021), 2100463.

[37] L.B. Rocha, G. Goissis, M.A. Rossi, Biocompatibility of anionic collagen matrix as scaffold for bone healing, Biomaterials 23 (2002) 449–456.

[38] V. Karageorgiou, D. Kaplan, Porosity of 3D biomaterial scaffolds and osteogenesis, Biomaterials 26 (2005) 5474–5491.

[39] L. Zhou, L. Fan, X. Yi, Z. Zhou, C. Liu, R. Fu, et al., Soft conducting polymer hydrogels cross-linked and doped by tannic acid for spinal cord injury repair, ACS Nano 12 (2018) 10957–10967.

[40] X. Liu, A.L. Miller, S. Park, B.E. Waletzki, Z. Zhou, A. Terzic, et al., Functionalized carbon nanotube and graphene oxide embedded electrically conductive hydrogel synergistically stimulates nerve cell differentiation, ACS Appl. Mater. Interfaces 9 (2017) 14677–14690.

[41] Z. Wang, C. Roberge, L.H. Dao, Y. Wan, G. Shi, M. Rouabhia, et al., In vivo evaluation of a novel electrically conductive polypyrrole/poly (d, l-lactide) composite and polypyrrole-coated poly (d, l-lactide-co-glycolide) membranes, J. Biomed. Mater. Res. Part A: An Official Journal of The Society for Biomaterials 70 (2004) 28–38. The Japanese Society for Biomaterials, and The Australian Society for Biomaterials and the Korean Society for Biomaterials.

[42] Q. Pei, R. Qian, Protonation and deprotonation of polypyrrole chain in aqueous solutions, Synth. Met. 45 (1991) 35–48.

[43] H. Raben, P.W. Kämmerer, R. Bader, U. van Rienen, Establishment of a numerical model to design an electro-stimulating system for a porcine mandibular critical size defect, Appl. Sci. 9 (2019) 2160.

[44] J. Yin, Q. Liu, J. Zhou, L. Zhang, Q. Zhang, R. Rao, et al., Self-assembled functional components-doped conductive polypyrrole composite hydrogels with enhanced electrochemical performances, RSC Adv. 10 (2020) 10546–10551.

[45] A. Ramanavicius, A. Finkelsteinas, H. Cesiulis, A. Ramanaviciene, Electrochemical impedance spectroscopy of polypyrrole based electrochemical immunosensor, Bioelectrochemistry 79 (2010) 11–16.

[46] S. Kulandaivalu, N. Suhaimi, Y. Sulaiman, Unveiling high specific energy supercapacitor from layer-by-layer assembled polypyrrole/graphene oxide| polypyrrole/manganese oxide electrode material, Sci. Rep. 9 (2019) 1–10.

[47] M. Wang, M. Cui, W. Liu, X. Liu, Highly dispersed conductive polypyrrole hydrogels as sensitive sensor for simultaneous determination of ascorbic acid, dopamine and uric acid, J. Electroanal. Chem. 832 (2019) 174–181.

[48] Q. Zhang, S. Beirne, K. Shu, D. Esrafilzadeh, X.-F. Huang, G.G. Wallace, Electrical stimulation with a conductive polymer promotes neurite outgrowth and synaptogenesis in primary cortical neurons in 3D, Sci. Rep. 8 (2018) 1–10.

[49] A. Schwab, R. Levato, M. D'Este, S. Piluso, D. Eglin, J. Malda, Printability and shape fidelity of bioinks in 3D bioprinting, Chem. Rev. 120 (2020) 11028–11055.

[50] A. Ribeiro, M.M. Blokzijl, R. Levato, C.W. Visser, M. Castilho, W.E. Hennink, et al., Assessing bioink shape fidelity to aid material development in 3D bioprinting, Biofabrication 10 (2017), 014102.

[51] A. Shafiee, M. McCune, G. Forgacs, I. Kosztin, Post-deposition bioink self-assembly: a quantitative study, Biofabrication 7 (2015), 045005.

[52] N. Paxton, W. Smolan, T. Böck, F. Melchels, J. Groll, T. Jungst, Proposal to assess printability of bioinks for extrusion-based bioprinting and evaluation of rheological properties governing bioprintability, Biofabrication 9 (2017), 044107.

[53] C.W. Peak, J. Stein, K.A. Gold, A.K. Gaharwar, Nanoengineered colloidal inks for 3D bioprinting, Langmuir 34 (2018) 917–925.

[54] Q. Gao, X. Niu, L. Shao, L. Zhou, Z. Lin, A. Sun, et al., 3D printing of complex GelMA-based scaffolds with nanoclay, Biofabrication 11 (2019), 035006.

[55] T. Gao, G.J. Gillispie, J.S. Copus, A.K. Pr, Y.-J. Seol, A. Atala, et al., Optimization of gelatin–alginate composite bioink printability using rheological parameters: a systematic approach, Biofabrication 10 (2018), 034106.

[56] L.-C. Gerhardt, A.R. Boccaccini, Bioactive glass and glass-ceramic scaffolds for bone tissue engineering, Materials 3 (2010) 3867–3910.

[57] A.H. Alomari, M.-L. Wille, C.M. Langton, Bone volume fraction and structural parameters for estimation of mechanical stiffness and failure load of human cancellous bone samples; in-vitro comparison of ultrasound transit time spectroscopy and X-ray μCT, Bone 107 (2018) 145–153.

[58] T. Orr, P. Villars, S. Mitchell, H.-P. Hsu, M. Spector, Compressive properties of cancellous bone defects in a rabbit model treated with particles of natural bone mineral and synthetic hydroxyapatite, Biomaterials 22 (2001) 1953–1959.

[59] H. Chen, J. Sun, Z. Wang, Y. Zhou, Z. Lou, B. Chen, et al., Magnetic cell–scaffold interface constructed by superparamagnetic IONP enhanced osteogenesis of adipose-derived stem cells, ACS Appl. Mater. Interfaces 10 (2018) 44279–44289.

[60] Z. Huang, Y. He, X. Chang, J. Liu, L. Yu, Y. Wu, et al., A Magnetic Iron Oxide/ Polydopamine Coating Can Improve Osteogenesis of 3D-Printed Porous Titanium Scaffolds with a Static Magnetic Field by Upregulating the TGFβ-Smads Pathway, Advanced healthcare materials 9 (2020) 1–13.

[61] A. Mondal, A. Gebeyehu, M. Miranda, D. Bahadur, N. Patel, S. Ramakrishnan, et al., Characterization and printability of sodium alginate-gelatin hydrogel for bioprinting NSCLC co-culture, Sci. Rep. 9 (2019) 1–12.

[62] L. Ouyang, J.P. Armstrong, Y. Lin, J.P. Wojciechowski, C. Lee-Reeves, D. Hachim, et al., Expanding and optimizing 3D bioprinting capabilities using complementary network bioinks, Sci. Adv. 6 (2020), eabc5529.

[63] H. Zhang, Y. Cong, A.R. Osi, Y. Zhou, F. Huang, R.P. Zaccaria, et al., Direct 3D printed biomimetic scaffolds based on hydrogel microparticles for cell spheroid growth, Adv. Funct. Mater. 30 (2020), 1910573.

[64] T.J. Hinton, Q. Jallerat, R.N. Palchesko, J.H. Park, M.S. Grodzicki, H.-J. Shue, et al., Three-dimensional printing of complex biological structures by freeform reversible embedding of suspended hydrogels, Sci. Adv. 1 (2015), e1500758.

[65] P. Li, X. Dou, C. Feng, H. Schönherr, Enhanced cell adhesion on a bio-inspired hierarchically structured polyester modified with gelatin-methacrylate, Biomater. Sci. 6 (2018) 785–792.

[66] M. Mahmoudi, C. Wang, S. Moreno, S.R. Burlison, D. Alatalo, F. Hassanipour, et al., Three-dimensional printing of ceramics through "carving" a gel and "filling in" the precursor polymer, ACS Appl. Mater. Interfaces 12 (2020) 31984–31991.

[67] Z. Luo, G. Tang, H. Ravanbakhsh, W. Li, M. Wang, X. Kuang, et al., Support bath-free vertical extrusion cryo (bio) printing for anisotropic tissue manufacturing, Adv. Mater. (2021), 2108931.

[68] Y. Zhang, L. Xu, Z. Liu, X. Cui, Z. Xiang, J. Bai, et al., Self-powered pulsed direct current stimulation system for enhancing osteogenesis in MC3T3-E1, Nano Energy 85 (2021), 106009.

[69] G. Thrivikraman, P.S. Lee, R. Hess, V. Haenchen, B. Basu, D. Scharnweber, Interplay of substrate conductivity, cellular microenvironment, and pulsatile electrical stimulation toward osteogenesis of human mesenchymal stem cells in vitro, ACS Appl. Mater. Interfaces 7 (2015) 23015–23028.

[70] Y. Wei, X. Mo, P. Zhang, Y. Li, J. Liao, Y. Li, et al., Directing stem cell differentiation via electrochemical reversible switching between nanotubes and nanotips of polypyrrole array, ACS Nano 11 (2017) 5915–5924.

[71] C. Ning, Z. Zhou, G. Tan, Y. Zhu, C. Mao, Electroactive polymers for tissue regeneration: developments and perspectives, Prog. Polym. Sci. 81 (2018) 144–162.

[72] J. Le, L. Zhongqun, W. Zhaoyan, S. Yijun, W. Yingjin, W. Yaojie, et al., Development of methods for detecting the fate of mesenchymal stem cells regulated by bone bioactive materials, Bioact. Mater. 6 (2021) 613–626.

[73] X. Wan, Z. Liu, L. Li, Manipulation of stem cells fates: the master and multifaceted roles of biophysical cues of biomaterials, Adv. Funct. Mater. 31 (2021), 2010626.

[74] T. Velletri, Y. Huang, Y. Wang, Q. Li, M. Hu, N. Xie, et al., Loss of p53 in mesenchymal stem cells promotes alteration of bone remodeling through negative regulation of osteoprotegerin, Cell Death Differ. 28 (2021) 156–169.

[75] L.A. Damiati, S. El-Messeiry, An overview of RNA-based scaffolds for osteogenesis, Front. Mol. Biosci. 8 (2021) 454.

[76] Z. Zhong, J. Wang, J. Tian, X. Deng, A. Balayan, Y. Sun, et al., Rapid 3D bioprinting of a multicellular model recapitulating pterygium microenvironment, Biomaterials 282 (2022), 121391.

[77] T.J. Bartosh, J.H. Ylöstalo, A. Mohammadipoor, N. Bazhanov, K. Coble, K. Claypool, et al., Aggregation of human mesenchymal stromal cells (MSCs) into 3D spheroids enhances their antiinflammatory properties, Proc. Natl. Acad. Sci. USA 107 (2010) 13724–13729.

[78] S. Wiedenmann, M. Breunig, J. Merkle, C. von Toerne, T. Georgiev, M. Moussus, et al., Single-cell-resolved differentiation of human induced pluripotent stem cells into pancreatic duct-like organoids on a microwell chip, Nature biomedical engineering 5 (2021) 897–913.

[79] P.M. George, T.M. Bliss, T. Hua, A. Lee, B. Oh, A. Levinson, et al., Electrical preconditioning of stem cells with a conductive polymer scaffold enhances stroke recovery, Biomaterials 142 (2017) 31–40.

[80] S.H. Llewellyn, A. Faroni, M. Iliut, C. Bartlam, A. Vijayaraghavan, A.J. Reid, Graphene oxide substrate promotes neurotrophic factor secretion and survival of human schwann-like adipose mesenchymal stromal cells, Advanced Biology 5 (2021), 2000271.

[81] M. Elsafadi, M. Manikandan, R. Dawud, N. Alajez, R. Hamam, M. Alfayez, et al., Transgelin is a TGFβ-inducible gene that regulates osteoblastic and adipogenic differentiation of human skeletal stem cells through actin cytoskeleston organization, Cell Death Dis. 7 (2016) e2321 (e).

[82] L. Li, W. Liu, H. Wang, Q. Yang, L. Zhang, F. Jin, et al., Mutual inhibition between HDAC9 and miR-17 regulates osteogenesis of human periodontal ligament stem cells in inflammatory conditions, Cell Death Dis. 9 (2018) 1–11.

[83] X. Zhu, J. Zuo, Y. Liu, R. Zang, Y. Li, X. Wang, et al., Osteogenesis of umbilical mesenchymal stem cells is enhanced in absence of DNA methyltransferase 3B

(DNMT3B) through upregulating Runx2 expression, Eur. Rev. Med. Pharmacol. Sci. 18 (2014) 3004–3009.
[84] G. Thrivikraman, S.K. Boda, B. Basu, Unraveling the mechanistic effects of electric field stimulation towards directing stem cell fate and function: a tissue engineering perspective, Biomaterials 150 (2018) 60–86.
[85] X. Tu, Y. Rhee, K.W. Condon, N. Bivi, M.R. Allen, D. Dwyer, et al., Sost downregulation and local Wnt signaling are required for the osteogenic response to mechanical loading, Bone 50 (2012) 209–217.
[86] H. Long, Y. Zhu, Z. Lin, J. Wan, L. Cheng, M. Zeng, et al., miR-381 modulates human bone mesenchymal stromal cells (BMSCs) osteogenesis via suppressing Wnt signaling pathway during atrophic nonunion development, Cell Death Dis. 10 (2019) 1–15.
[87] H. Nikukar, S. Reid, P.M. Tsimbouri, M.O. Riehle, A.S. Curtis, M.J. Dalby, Osteogenesis of mesenchymal stem cells by nanoscale mechanotransduction, ACS Nano 7 (2013) 2758–2767.
[88] D. Khare, B. Basu, A.K. Dubey, Electrical stimulation and piezoelectric biomaterials for bone tissue engineering applications, Biomaterials 258 (2020), 120280.
[89] M. Guillot-Ferriols, S. Lanceros-Méndez, J.G. Ribelles, G.G. Ferrer, Electrical stimulation: effective cue to direct osteogenic differentiation of mesenchymal stem cells? Biomaterials Advances (2022), 212918.